

LAPPEENRANTA-LAHTI UNIVERSITY OF TECHNOLOGY LUT  
School of Energy Systems  
Electrical Engineering

*Tuukka Nurminen*

# ANALYTIC DESIGN METHODOLOGY FOR HOMOPOLAR MAGNETIC BEARING WITH PERMANENT MAGNET BIASING

Examiners: Professor Juha Pyrhönen  
D.Sc. Alexander Smirnov

## **ABSTRACT**

Lappeenranta-Lahti University of Technology LUT  
School of Energy Systems  
Electrical Engineering

Tuukka Nurminen

### **Analytical Design Methodology for Homopolar Magnetic Bearing with Permanent Magnet Biasing**

Master's thesis

2020

64 pages, 27 figures and 8 tables

Examiners: Professor J.P. and D.Sc. (Tech.) A.S.

Keywords: Magnetic bearing, geometry, reluctance, FEM

There are several factors that can be varied in the design of an active magnetic bearing (AMB). These include, how the magnetic poles are arranged, how the bias flux is generated and in which direction the carrying force is needed. Homopolar AMB with permanent magnet (PM) biasing brings lots of benefits into compared to typical AMB systems. Most importantly the permanent magnet provides higher energy efficiency in form of “free” bias flux generation.

The design of a homopolar AMB with PM biasing starts with calculation of the geometry of the actuator. With the geometry values a 3D-model is created which is imported to a finite element method (FEM) calculation software for more detailed analysis. The system can also be analysed analytically. The analytical analysis is done by estimating the main reluctances which include leakages and the reluctances of the materials. The error in the analytical model is monitored with a reference FEM model which gives an idea if the values of the model are any good.

After the analytical analysis of the AMB more detailed 3D-FEM calculation can be performed for verification purposes. The most limiting factor of 3D-FEM analysis is that it is very time and calculation power intensive. To solve this problem a transformation is done to the  $BH$ -curve and the space factor of the laminated material to consider the effect of the slots in 3D model. These transformations provide flux values which represent the 3D-environment in 2D-model.

The obtained result was ~10% maximum error between the analytical and FEM-calculations. In addition, with the modified 2D-FEM model the results differentiate only by a couple of percent from the full 3D-FEM calculations. Also, the calculation effort with the 2D-model is reduced to only a small fraction of the one done with the 3D-model.

## **Tiivistelmä**

Lappeenrannan-Lahden Teknillinen Yliopisto LUT  
School of Energy Systems  
Sähkötekniikka

Tuukka Nurminen

### **Analytical Design Methodology for Homopolar Magnetic Bearing with Permanent Magnet Biasing**

Diplomityö

2020

64 sivua, 27 kuvaajaa and 8 taulukkoa

Tarkastajat: Professor J.P. and D.Sc. (Tech.) A.S.

Avainsanat: Magneettilaakerit, geometria, reluktanssi, FEM

Aktiivi-magneettilaakereiden (AMB) suunnittelussa on olemassa muutama päälähtökohta. Näitä ovat esimerkiksi se missä järjestyksessä magneettiset navat ovat, miten esimagnetointi on järjestetty ja mihin suuntaan laakerin tuottama päävoimavektorin tulisi olla. Homopolaarinen kestopagnetoitu AMB-malli tuo mukanaan monenlaisia etuja verrattuna perinteisiin aktiivi magneettilaakereihin. Tärkein näistä eduista on, että kestopagneetti synnyttää laakerin esimagnetoinnin ilman erillistä energiaa.

Homopolaarisen magneettilaakerin suunnittelu alkaa sen osien geometrioiden laskemisella. Kun laakerin geometria on saatu laskettua siitä, voidaan luoda 3D-malli, joka voidaan esimerkiksi syöttää FEM-laskentaohjelmaan tarkempaa analyysiä varten. Tämä analysointi voidaan suorittaa myös analyyttisesti. Analyyttinen malli perustuu systeemin pääreluktanssien (vuotokohtien - ja materiaalien reluktanssien) estimoimiseen. Analyyttisen mallin synnyttämää virhettä seurataan vertaamalla analyyttisen mallin tuloksia FEM-laskennasta saatuihin tuloksiin. Tämä virheenseuranta antaa myös kuvan siitä onko käytetty analyysimenetelmä hyvä vai huono.

Laakerin analysoinnin jälkeen suoritetaan tarkempi 3D-FEM analyysi, jotta käytetyt analysointimenetelmät voidaan todentaa todellisuutta vastaaviksi. 3D-FEM analyysiä pyritään välttämään, koska se vaatii paljon aikaa ja sitoo paljon laskentakapasiteettia. Tämän ratkaisemiseksi käytettyjen materiaalien  $BH$ -käyriä muutetaan siten että ne saadaan vastaamaan paremmin 3D-vuojakaumaa. Myös laminaattimateriaalin tilakerroita muokataan paremmin sopivaksi. Näiden muokkausten avulla pystytään luomaan 2D-FEM malli, jonka tuottamat magneettivuon arvot vastaavat 3D-mallia.

Lopputulokseksi saatiin noin 10 %:n virhe analyyttisen- ja FEM-mallin tulosten välillä. Myös muokatun 2D-FEM mallin ja 3D-FEM mallin tulosten väliseksi virheeksi saatiin vain muutama prosentti. Tämän lisäksi 2D-FEM mallin tarvitsema laskentakapasiteetti on vain murto-osa siitä, mitä 3D-FEM malli tarvitsee.

## LIST OF SYMBOLS AND ABBREVIATIONS

### Symbols

$A$	Surface area [m <sup>2</sup> ]
$A_{\text{coil}}$	Area of the coil [m <sup>2</sup> ]
$A_{\text{pm}}$	Total area of a split magnet pieces [m <sup>2</sup> ]
$A_{\text{pole}}$	Surface area of a pole [m <sup>2</sup> ]
$b_1$	Width of the slot opening [mm]
$b_2$	Width of the slot shoulder [mm]
$b_3$	Width of the back end of the slot [mm]
$B_{\text{bias}}$	Bias flux of the system
$B_{\text{dl}}$	Flux density at the dead leg air gap [T]
$B_{\text{dl,ref}}$	Reference value for flux density at the dead leg air gap [T]
$B_{\text{lam}}$	Flux density at the stator air gap [T]
$B_{\text{lam,ref}}$	Reference value for flux density at the stator air gap [T]
$B_r$	Remanence of the permanent magnet [T]
$B_{\text{sat}}$	Saturation Flux density of a steel material used [T]
$C_f$	Friction coefficient
$F_{\text{avg}}$	Average Force [N]
$F_{\text{max}}$	Maximum Force [N]
$F_{\text{pm}}$	Magnetomotive force of a permanent magnet [A]
$f_r$	Frequency level of the system [Hz]
$f_x$	Force as a function of control current and displacement [N]
$g$	Standard acceleration due to gravity [m/s <sup>2</sup> ]
$g_0$	Air gap [mm]
$h_1$	Height of the slot opening [mm]
$H_c$	Coercivity of the magnet [A/m]
$I_c$	Control current [A]
$I_{\text{max}}$	Maximum current of the system [A]
$I_{\text{rms}}$	Root mean square current of the system [A]
$J_{\text{Cu}}$	Current density of copper [A/m <sup>2</sup> ]
$k$	Mechanical stiffness [N/m]
$k_{\text{Cu}}$	Copper space factor
$k_{\text{Fe}}$	Iron ratio

$k_i$	Force-current factor [N/A]
$k_{pm}$	Permanent magnet packing factor
$K_{pole,0}$	Pole factor/iron factor at the air gap level
$k_x$	Force-displacement factor [N/mm]
$l$	Length [mm]
$l_{amb}$	Total length of the AMB [mm]
$L_{coil}$	Inductance of a coil [mH]
$l_{coil}$	Length of the coil [mm]
$l_{coil,end}$	Length of the end winding [mm]
$l_d$	Peripheral length of the dead leg [mm]
$l_{d,down}$	Length of the lower part of the dead leg [mm]
$l_{d,up}$	Length of the upper part of the dead leg [mm]
$l_{pm}$	Length of the permanent magnet [mm]
$l_{pole}$	Peripheral length of the pole [mm]
$l_{stack}$	Length of the lamination stack [mm]
$m$	Mass [kg]
$n$	Number of poles
$N$	Number of turns
$P_{Cu}$	Copper losses of the system [W]
$P_w$	Aerodynamic losses in the systems air gap [W]
$R$	Resistance [ $\Omega$ ]
$R_{coil}$	Resistance of a coil [ $\Omega$ ]
$R_{m,cyl}$	Reluctance of the first circuit iteration [1/H]
$R_{m,dl}$	Reluctance of the dead leg air gap [1/H]
$R_{m,dl,ac}$	Reluctance between the stator and the dead leg [1/H]
$R_{m,dl,fr}$	Reluctance of the dead leg air gap when fringing is considered [1/H]
$R_{m,dleg}$	Reluctance of the solid dead leg [1/H]
$R_{m,fr}$	Total reluctance of single pole fringing [1/H]
$R_{m,lam}$	Reluctance of the stator air gap [1/H]
$R_{m,lam,fr}$	Reluctance of the stator air gap when fringing is considered [1/H]
$R_{m,lam,pole}$	Reluctance of single stator pole air gap [1/H]
$R_{m,lam,pole,fr}$	Total reluctance of single stator pole air gap when fringing is considered [1/H]
$R_{m,lamleg}$	Reluctance of the solid stator [1/H]

$R_{m,pm}$	Reluctance of the permanent magnet [1/H]
$R_{m,pm,top1}$	Reluctance of the leakage path just above the magnet [1/H]
$R_{m,pm,top2}$	Reluctance of the leakage path just above $R_{m,pm,top1}$ [1/H]
$R_{m,side}$	Reluctance of the side leakage path [1/H]
$r_{pm,i}$	Radius to the inner edge of the permanent magnet [mm]
$r_{pole}$	Radius of the AMB to the pole surface [mm]
$r_{re}$	Rotor external radius [mm]
$r_{ri}$	Rotor internal radius [mm]
$r_{se}$	Stator external radius [mm]
$r_{slot}$	Radius of the AMB to the back of the slot [mm]
$S_{pm}$	Area of a solid permanent magnet ring [m <sup>2</sup> ]
$S_{wire}$	Cross-sectional area of a coil wire [m <sup>2</sup> ]
$x$	Rotor displacement [μm]
$x_0$	Zero position for the rotor
$\mu_0$	Permeability of vacuum [H/m]
$\mu_{pm}$	Relative permeability of a permanent magnet [H/m]
$\mu_r$	Relative permeability of a material [H/m]
$\rho$	Resistivity [Ωm]
$\rho_{air}$	Density of air [kg/m <sup>3</sup> ]
$\phi$	Magnetic flux [Wb]
$\phi_{lam}$	Flux in the laminated material [Wb]
$\omega$	Rotation frequency of the system [rad/s]
$\omega_1$	First bending angular velocity [rad/s]
$\omega_r$	Critical speed of the system [rad/s]

## Abbreviations

AMB	Active Magnetic Bearing
CNC	Computer Numerical Control
CAD	Computer Aided Design
EM	Electrical machine
FEM	Finite element method
NdFeB	Neodymium boron iron
PM	Permanent magnet
RMS	Root mean Square

## **ACKNOWLEDGEMENTS**

This master's thesis was made for the Spin Drive Ltd. I would like to thank SpinDrive for such an interesting subject for my thesis. Also, I would like to thank people at SpinDrive for providing exceptional working environment in which to work on my thesis. Special thanks to my supervisor and examiner CTO Alexander Smirnov of SpinDrive for providing with a lot of valuable information and help when needed.

Thanks to professor Juha Pyrhönen for the examination and for providing valuable tips for the overall structure of the thesis. The teaching staff at LUT-university gets a special mention for the great work they have put into the teaching during these past years. Lastly, I would like to thank all my friends and family for the great support they have provided during my studies.

## TABLE OF CONTENTS

List of Symbols and Abbreviations .....	3
1. Introduction.....	6
1.1 Background and Relevance of the Work .....	6
1.2 Purpose and Goal of the Work.....	8
2. Design Choices for the Active Magnetic Bearing .....	9
2.1 AMB Design Choice Comparison .....	11
2.1.1 Heteropolar or Homopolar Composition.....	11
2.1.2 Bias flux generation .....	13
2.1.3 Type of AMB .....	15
2.2 Magnetic Circuit of the Homopolar Radial AMB with Permanent Magnet Biasing 17	
3. Bearing Design Procedure .....	20
3.1 Geometry of the AMB .....	20
3.1.1 Stator Yoke.....	22
3.1.2 Slot Geometry .....	23
3.1.3 Dead Leg .....	25
3.1.4 Permanent Magnet.....	25
3.1.5 Coil Parameters .....	27
3.2 Reluctances, Force-Current Factor, and Force-Displacement Factor of the AMB..	28
3.2.1 Reluctances of the Air Gaps and of the PM .....	29
3.2.2 Main Leakage Reluctances.....	30
3.2.3 Fringing and Reluctance of the Steel Parts .....	31
3.2.4 Side Leakages.....	32
3.2.5 Separation of the Fluxes .....	33
3.2.6 Force Production and Force-Current and Force-Displacement Factors .....	34



4.	Optimization of the Bearing.....	35
4.1	Objective Function.....	36
4.2	Optimization Parameters.....	38
4.3	Optimization Algorithm.....	38
4.4	Optimization Example .....	39
5.	Verification of results with FEM .....	44
5.1	Testing the Viability of the Model.....	44
5.2	Static 3D FEM Analysis of the Homopolar AMB with PM Biasing.....	47
5.2.1	Bias flux in the system .....	49
5.2.2	Bearing capacity of the AMB.....	51
5.2.3	Laminated material.....	53
5.3	Measures Needed to Avoid 3D-FEM Analysis .....	54
5.3.1	Calculation of Negative Stiffness.....	59
6.	Conclusions and Suggestions for Future Work .....	61
Sources	63	

# **1. INTRODUCTION**

## **1.1 Background and Relevance of the Work**

As demand for more power-dense electric motors increases, interest in raising the nominal speeds of motors also increases. This is because of the quasi-linear relation between the shaft power and rotational speed which makes increasing the rated speed of the electrical motor an effective way to increase power density and efficiency. As the rotational speed of the system increases, the requirements for the bearings increases.

When the rotational speed is increased, the traditional way is to use oil lubricated ceramic ball bearings or sliding bearings in a high-speed system. A high-speed system is classified as a system where the tangential speed of the rotor surface is above 200 m/s. The problem with mechanical bearings in a high-speed system is that they are the most probable cause for failures increasing the downtime of the whole system. Another downside of a mechanical bearing is the need for regular maintenance which increases the life cycle costs of the system.

Magnetic bearings are another consideration for the high-speed systems. Magnetic bearings can be classified either as active or passive depending on whether there is control supporting the operation or not. Passive magnetic bearings are rarely used, as their use is limited by low force capacity and small damping. Active magnetic bearings (AMBs) however are on a raising trend as they can bring many benefits over traditional mechanical bearings.

Active magnetic bearings bring interesting opportunities when compared with traditional mechanical bearings. These include contactless rotor support (eliminating mechanical wear and the need for lubricants), ability to fine tune bearing parameters on the software side to optimize system performance, eliminating the need for oil or other hazardous material based lubricants and opportunities with remote monitoring and health diagnostics, etc. The main problem with AMBs is that they must be designed separately for each application and that they need a relatively large space which easily affects the rotor dynamics adversely. The engineering work makes the cost of singular units high while the hardware cost is low.

AMB at the system level consists of the following components: an electromagnetic actuator with integrated position sensors, power amplifier and controller. Control of the AMB is based on the feedback from the position sensor. Controller then feeds reference currents for the power amplifier which supplies the currents into the electromagnets where they are converted into required forces.

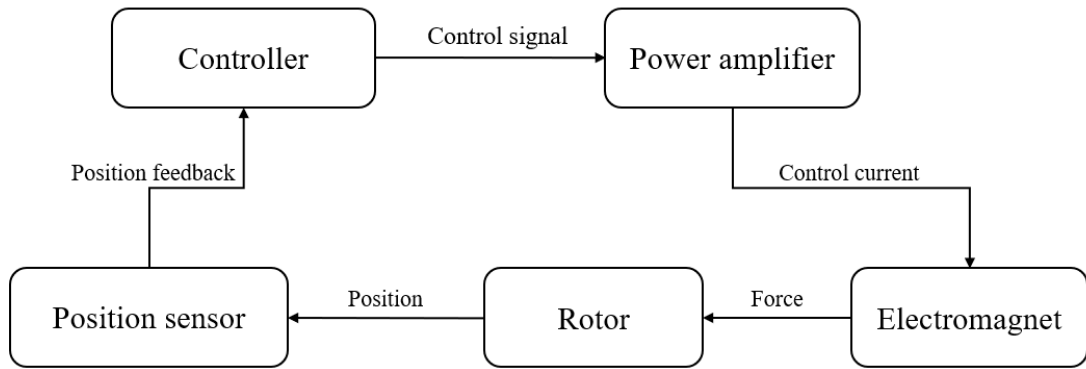


**Figure 1-1** Operation loop of an AMB system

The aim in the AMB operation is to produce correct magnetic forces for the rotor. A single magnetic force of the AMB with current control is a function of control current  $i$  and rotor displacement  $x$ . Also, a force-current  $k_i$  and a force-displacement  $k_s$  factors are introduced which depict the system behaviour with respect to the variables  $i$  and  $x$ . These factors are fundamental to the control side of the AMB system as they linearize the system behaviour.

The mechanical stiffness  $k$  of the system is a negative derivative of the suspension force  $F$  and displacement:  $k = -\frac{\partial F}{\partial x}$ . However because the magnetic suspension force works opposite to the mechanical one (it increases the closer the object is with the magnet) the stiffness of the AMB is negative. The levitation in the AMB system is achieved with a constant adjusting of the control current so that the rotor is kept in the desired position  $x_0$ . The position is measured with position sensors which are most commonly eddy current proximity probes. Hall sensors or

solid-state sensors are used to measuring the flux of the system. In an AMB system there is also a mechanical bearing called *touch-down bearing* as a safety feature in case of a failure in the system which is typically either a power failure or load saturation of the AMB.

As the engineering costs of the AMBs are high, their usage is still quite limited. AMBs have found use in applications such as turbo compressors, turbo blowers, flywheels, CNC machines and Organic Rankine Cycle units. In the future as more and more technologies looking for ways to increase the energy efficiency even further, AMBs bring much to the table. On the general level AMBs are also dependent on the development of the design methods to reduce the engineering costs of the AMB.

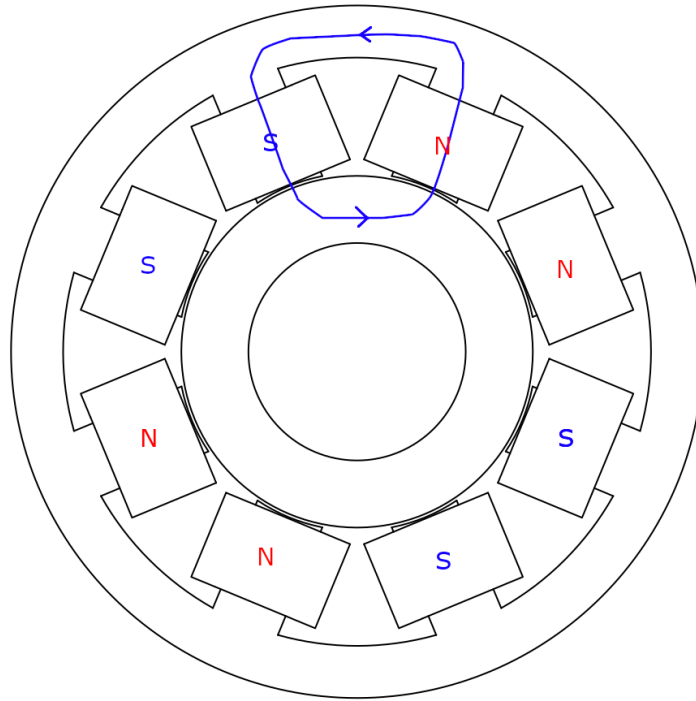
## **1.2 Purpose and Goal of the Work**

The purpose of this work is to develop a straightforward methodology for the analytical dimensioning of the homopolar magnetic bearing circuit based on the input requirements. This should provide a fast and agile method to be used in the overall design of the system. The analytical model gives fast and computationally efficient results when compared with FEM which is used only to verify the results got from the analytical model. By doing this the effort and time required to obtain the final system parameters are reduced significantly.

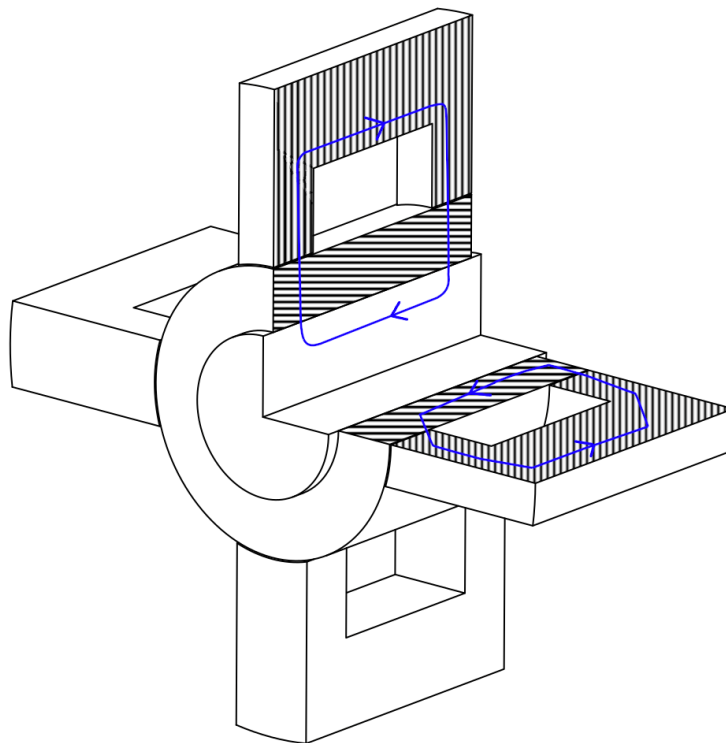
The goal in this work is to derive an analytical model which provides results with ~10 % error margin when compared with the FEM-calculation results. This result would ensure that the results from the analytical model could be used as such if needed.

## **2. DESIGN CHOICES FOR THE ACTIVE MAGNETIC BEARING**

There are multiple fundamental decisions that need to be made when starting the design of the AMB system. These include the composition of the magnetic poles, bias flux generating method and direction of the bearing force. All of these affect the construction of the AMB significantly. There are two compositions for arranging the magnetic poles for active magnetic bearings (AMBs) heteropolar or homopolar. In the heteropolar design the polarity of the stator poles vary along the rotational plane. In the homopolar design pole polarities are the same. Another way to distinguish the AMBs is how the bias flux is generated in the system. AMBs can also be sorted by the direction of the primary force vector like in mechanical bearings: radial- and axial magnetic bearings. These two can also be combined into a single magnetic bearing in a “side by side” design. In this work, the focus is on the homopolar permanent magnet biased active magnetic bearing design. In this chapter, different factors which affect the construction of the AMB are gone through. The reluctance network which is the basis for the magnetic circuit analysis is also presented.



a)



b)

**Figure 2-1** Examples of heteropolar - and homopolar radial AMB compositions. Blue lines indicate a bias flux travel path

## 2.1 AMB Design Choice Comparison

### 2.1.1 Heteropolar or Homopolar Composition

As stated above, there are two ways to arrange the magnetic poles inside the AMB, hetero- or homopolar. For radial loads, the heteropolar composition has been the choice to go with as it is much simpler construction-wise and thus the analysis of the magnetic circuit is much simpler. In terms of axial loads, the homopolar composition has been the natural choice because of the direction of the required force vector. However, as the analysis methods have developed the homopolar composition has been adapted to the radial load side as well. This is because the homopolar composition brings significant advantages to the table over heteropolar.

The main advantage of the homopolar composition for AMB over the heteropolar construction is that there will be much less variation of the magnetic flux density in the rotor while spinning because there is no change in the bias pole polarity around the actuator axis in any given axial plane. In addition, with or without radial load a homopolar design will induce less eddy currents in the rotor while the rotor is spinning.

With the designs shown in Figure 2-1 the heteropolar design performs better with time varying radial loads. This is because of the control flux in the heteropolar bearing that flows in the laminated plane and thus eddy currents are minimized.

In the general case, to best utilize laminated material the time varying magnetic flux should flow in the direction of the lamination. When taking the highest advantage of the laminated material, insulation between lamination layers will block the eddy currents which are induced by the altering flux as dictated by the Faraday's law. Also, because the effective surface area of a single lamination layer will be much smaller, the resistance affecting the eddy currents will be a lot higher because of  $R = \frac{\rho l}{A}$  where  $R$  is the resistance,  $\rho$  is the resistivity of the material,  $l$  is the length of the object and  $A$  is the cross-sectional surface area.

In the homopolar design the control flux path will travel perpendicularly through the lamination planes partially. Eddy currents induced during this part would flow freely in either solid steel

or within the lamination planes. These currents would then produce their own magnetic fields countering the original control field and it would be driven into the edges because of the skin effect. All this would result in the reduction of the load capacity of the homopolar design compared with a similar volume heteropolar design. There will also be a phase lag between the control current and the force produced because of eddy currents.

This disadvantage with time varying loads on homopolar AMBs can be mitigated by changing the construction. An example of such a construction is illustrated in Figure 2-2 Cut-away drawing of PM-biased radial homopolar AMB. In that design, a permanent magnet is used to create the bias flux. PM is placed directly next to the laminated part so that the flux generated by the magnet must pass the lamination stacks before proceeding to the rotor. Problems with time varying loads are addressed by the control flux which only exists in the laminated part. The case where the bias flux must be pushed perpendicular to the lamination only affects the sizing of the permanent magnet and the flux distribution in the air gap.

The other leg which is non laminated is called ‘dead leg’ and serves as a travel path to the flux. To reduce the flux density in the air gap the lower end of the dead leg is widened. Also, in most cases the dead leg is fitted under the end winding of the electrical machine to reduce the overall axial length needed. This design also provides loss reduction when compared with the homopolar design. The electromagnetic losses and thus total losses of the system are reduced. Losses are reduced because of “free” and lossless bias flux generation by the permanent magnet, the low distribution of the air gap flux density harmonics and very low resistive losses in the control coil. The main issue with the design presented in Figure 2-2 is that the analysis of the system is by its nature a 3D-problem and thus can be time-consuming.



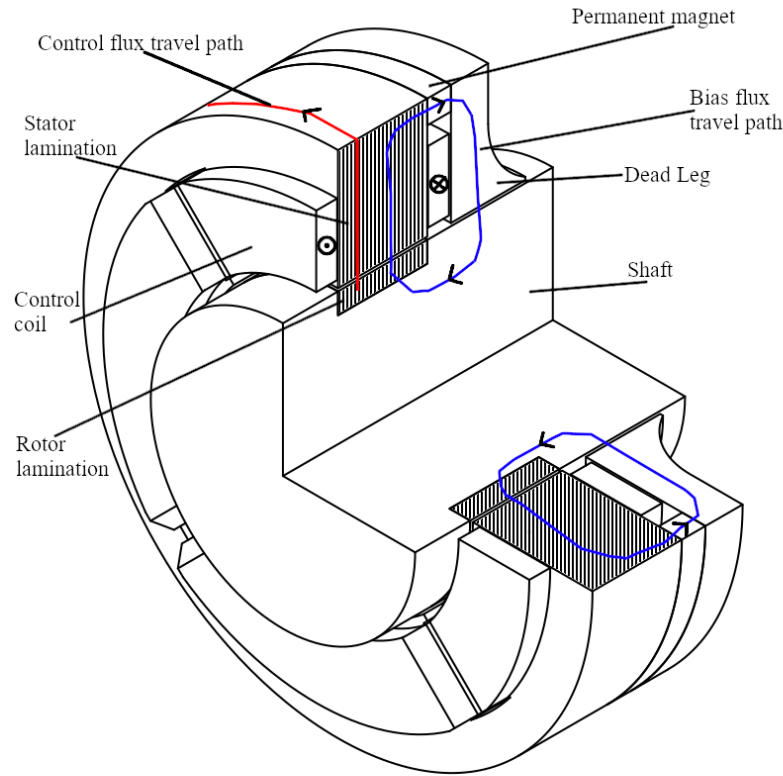


**Figure 2-2** Cut-away drawing of PM-biased radial homopolar AMB

### 2.1.2 Bias flux generation

In addition to heteropolar or homopolar basic design, the way the bias flux of the AMB is generated can be varied. The main purpose of the bias flux is to linearize the system behaviour and more detailed analysis of this behaviour is presented by (Filatov et. al. 2016) or by (Schwitzer et al. 2009, p. 79-81). Originally, this is done using coils for generating the bias flux. In this case, the bias and control flux are going through the same path. In homopolar design with PM biasing, however, these fluxes are partially separated which is one of the reasons why that design performs better compared to homopolar design presented in Figure 2-1(b). This separation of fluxes is displayed in Figure 2-3. Typically, the permanent magnet displayed in Figure 2-2 is not a solid ring but is constructed from smaller magnet pieces as they are much easier and cheaper to manufacture and thus are more widely available.

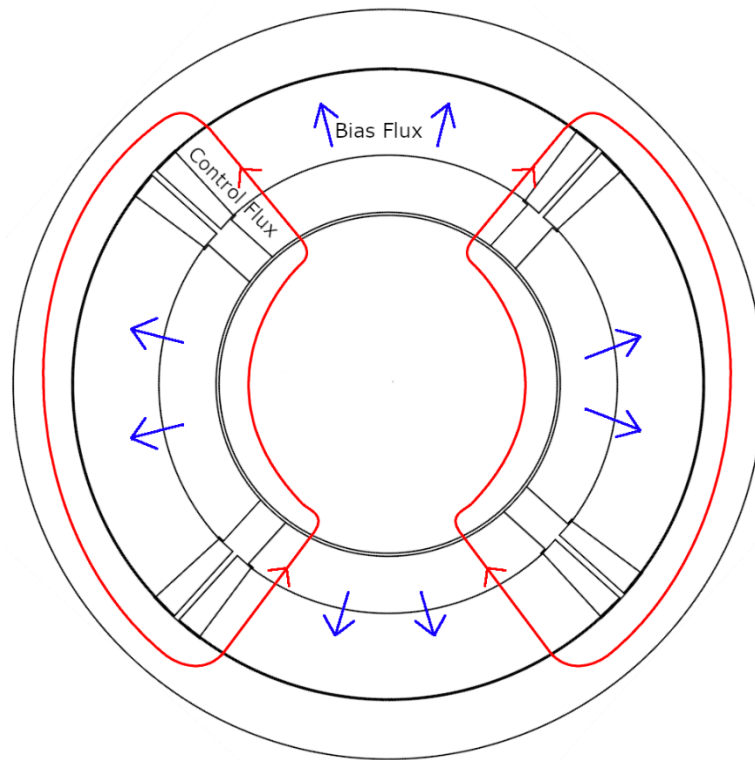


**Figure 2-3** Flux travel paths in the homopolar AMB with PM biasing

The permanent magnet provides benefits in form of energy savings as the bias flux is now generated without current. This lack of current also means that there is no need for an amplifier for the bias circuit. With the permanent magnet, typically the same bias flux can be created in the magnetic circuit in a smaller form factor than with coils. Negative stiffness will be much smaller in the bias circuit because of the large internal reluctance of the magnet (Filatov et al. 2014). If the homopolar design with PM bias is used, problems that have come up with other PM-based actuators are solved. These include the size of the coil and risk of demagnetization of the permanent magnet with the control current. These problems are solved because the control flux generated by the control coils does not travel through the permanent magnet. The control coil size is reduced as only control flux must be produced. Risk of demagnetization becomes apparent in design where the control field travels through the magnet. Because of the high internal reluctance of the magnet, it is made thin with a large surface area. By doing this the need to increase the control coil size is reduced while still are able to produce the required bias flux level.

The main disadvantage of the permanent magnets is that they are expensive especially if rare-earth magnets such as NdFeB magnets are used. Luckily in this design the temperature fluctuation is not a problem and thus lower quality magnets can be used, but they are still more expensive than coils. Despite low temperature fluctuation it is good to prepare just in case for the temperature rise because it can reduce the gain and lower the load capacity.

Another disadvantage with using the permanent magnets in AMBs is that their flux changes over time. The eddy currents induced by the changing control current in the windings deteriorate the PMs characteristics and thus change the bias flux produced by the PM. One suggested way to fight this is to place the PM on the rotor side. More detailed analysis of this design is presented in (Ismagilov et al. 2018).

Another magnet option used in the AMB is ferrite magnets. Ferrite magnets have a lot lower remanence and coercivity when compared with NdFeB -magnets, but they are much cheaper, and they are more resilient to corrosion and temperature changes. The main problem with ferrite magnets is that when used they need to be much larger to produce enough flux and thus, they increase the overall size of the AMB construction. Another general thing to consider when using any type of PMs is that the assembly with them is more difficult because the PMs cannot be “turned off”.

### 2.1.3 Type of AMB

As with the traditional mechanical bearings, there are major changes in the construction with active magnetic bearings depending on the direction of the main carrying force needed. So far in this thesis the focus has been on radial AMBs but axial AMBs are also needed. Axial AMB is typically constructed with homopolar composition because it is much simpler in design. Heteropolar composition does not bring any clear benefits to axial AMBs. Axial and radial AMB designs can be combined into single “side by side” actuator. Combining the carrying forces bring benefits in shorter axial length, lower part count and nearly constant and lower negative stiffness (Filatov et al. 2016). The main disadvantage of side by side AMB design is that it provides added complexity for the structure.

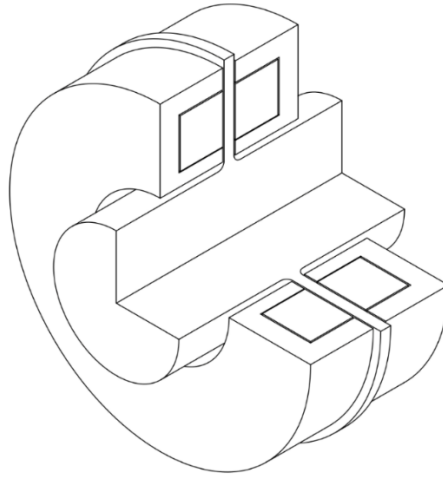


**Figure 2-4** Example of axial AMB design. There is a solid disk in between two coil arrangements

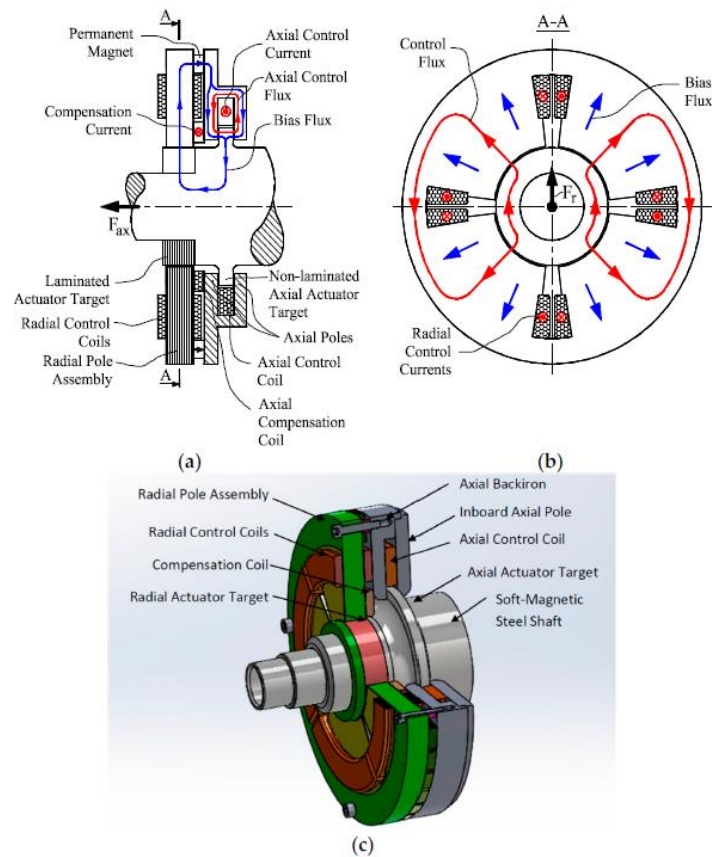


**Figure 2-5** “Side by side” Homopolar PM-biased combination Radial/Axial AMB Actuator by Calnetix Technologies LLC. (a) Axial cut-out section and axial channel operating principle; (b) Radial cross-section and radial channel operating principle; (c) 3D rendering. (Filatov, et al. 2016) Figure reproduced with the open-access-based permission by MDPI

## 2.2 Magnetic Circuit of the Homopolar Radial AMB with Permanent Magnet Biasing

This chapter is focusing on the radial homopolar AMB with permanent magnet biasing. An example of such a bearing is presented in Figure 2-2 Cut-away drawing of PM-biased radial homopolar AMB. Because of its construction, the flux distribution is 3-dimensional in the AMB. In addition, there are more opportunities for leakage paths in the construction which must be considered when constructing the equivalent reluctance circuit. These points do the analysis of the magnetic circuit more complicated with homopolar AMB than with heteropolar AMB. In Chapter 5, more about potential ways are discussed to minimize the need for 3-dimensional calculations during the design process. The main leakages of the magnetic circuit are illustrated in Figure 2-6. Analysis of the system is based on the reluctance circuit presented in Figure 2-7.

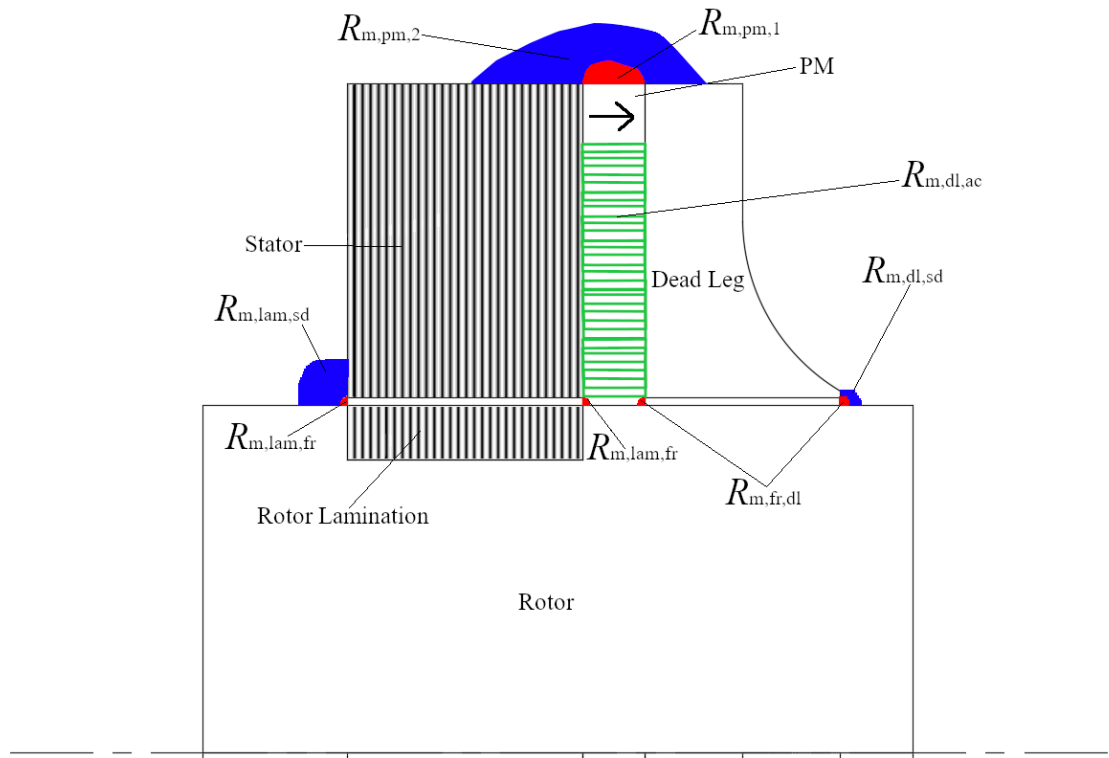


**Figure 2-6** Main leakages of the system

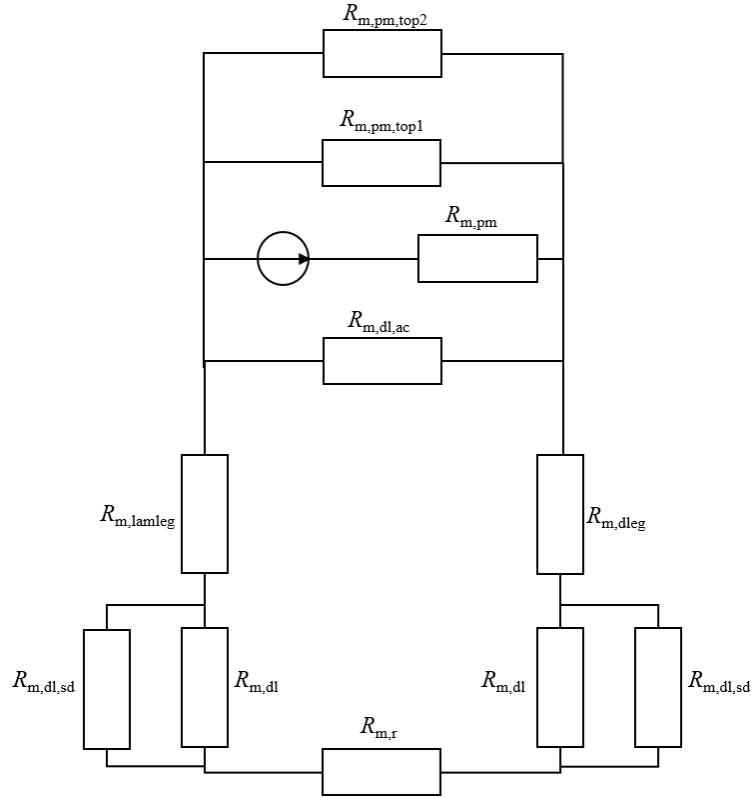


**Figure 2-7** Reluctance circuit for analysis of the homopolar AMB with PM biasing

Reluctance circuit presented in the Figure 2-7 Reluctance circuit for analysis of the includes following reluctances

$R_{m,pm}$	- Reluctance of the permanent magnet
$R_{m,pm\_top1}$ and $R_{m,pm\_top2}$	- Reluctances of the top portion of the permanent magnet
$R_{m,dl\_ac}$	- Reluctance between the legs
$R_{m,dleg}$	- Reluctance of the solid steel dead leg
$R_{m,lamleg}$	- Reluctance of the laminated stator pole

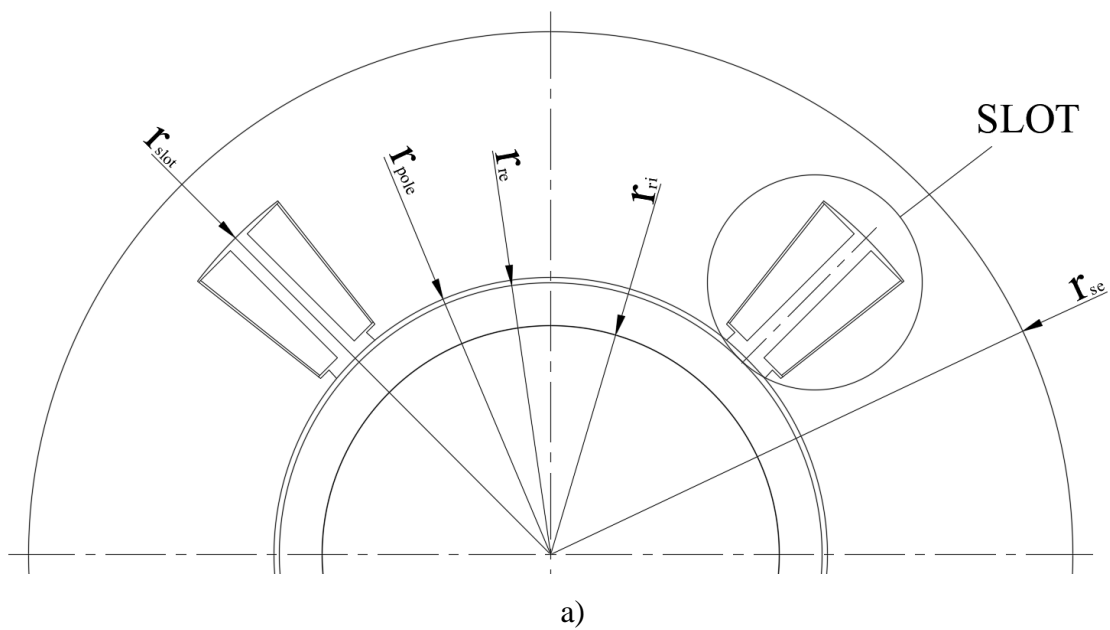
$R_{m,dl}$	- Reluctance of the air gap between dead leg and rotor with fringing
$R_{m,lam}$	- Reluctance of the air gap between stator and rotor with fringing
$R_{m,dl,sd}$ and $R_{m,lam,sd}$	- Reluctance of the side leakage
$R_{m,r}$	- Reluctance of the rotor ring

Calculation of these reluctances gives a good estimation of the magnetic voltage drop inside the magnetic circuit which enables estimating the flux in the air gaps. The reluctance network presented in Figure 2-7 includes only the most prominent leakages in the system that should give a reasonably accurate result. The selection of these reluctances is based on reference FEM-calculation which gives a good idea about the flux travel paths inside the system.

### 3. BEARING DESIGN PROCEDURE

The design of homopolar AMB with PM-biasing starts with constructing an analytical model which is used to determine the main dimensions of the AMB. Some basic reference values such as coil parameters (the number of turns, the length of the wire, inductance, and resistance of the coil, etc.) are estimated. At the end, the reluctance and fluxes of the system are calculated and with those the force production and force-current and force-displacement factors of the AMB are estimated. After the finishing, the calculation of the dimensions, the appropriate 3D-model can be drawn with a CAD-software. When, a dimensioned 3D-drawing of the system has been created it can be transferred into FEM-calculation software for more detailed analysis.

#### 3.1 Geometry of the AMB





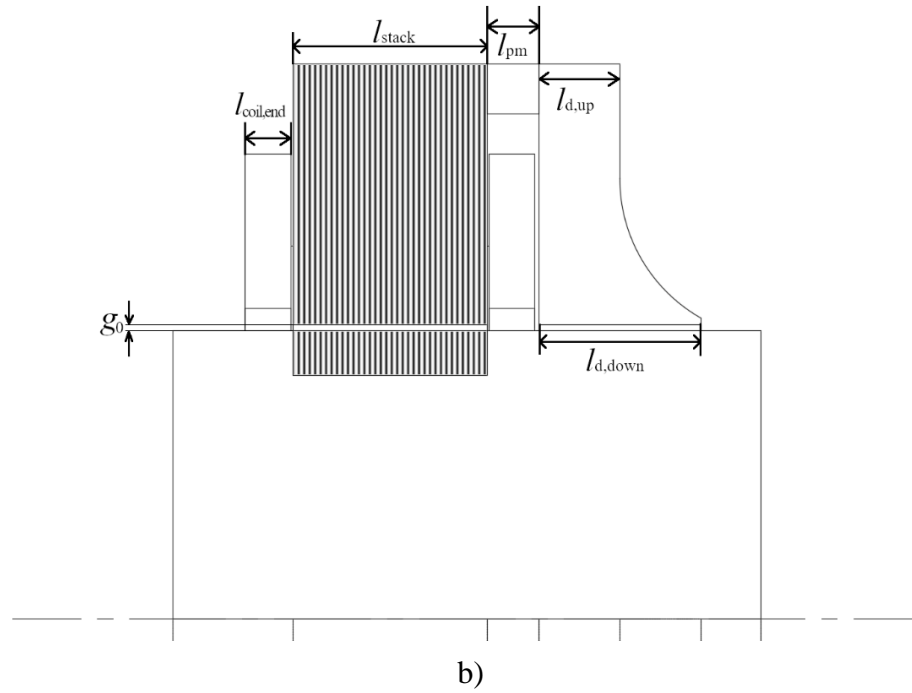


**Figure 3-1** Main dimensions of the homopolar AMB with PM-biasing. Where a) is cutaway view from front and b) is cutaway view from side

The radius of the rotor is usually already known because it is typically designed separately of the AMB. Tolerances for the joint between the rotor lamination and the shaft are set in the ISO-286 standard. The thickness of the rotor lamination is not set and the durability of it is mostly dependent on the material used. Another limiting factor for the rotor lamination material is heat resistance. This is, because the rotor is assembled with method called “shrink fitting”, where the shaft is shrunk under low temperature and/or the rotor lamination is expanded with heat. Thus, the insulation of the lamination material needs to be suitable for such conditions. When, parts are returned to normal temperatures, a very tight joint will form between the rotor lamination and the shaft. The required fit is dependent on the operation conditions (the temperature & rotational speed) which determine the expansion of the parts joint together.

The value of the air gap length is also set at one value although it is very difficult to set the exact value of the air gap because material surfaces will always have some flaws that affect the length of the air gap. Benefits provided by a smaller gap include lower control current and lower copper losses, but the requirements for the control system and manufacturing increase significantly.

For the other dimensional values, some input parameters are required, which include: maximum force  $F_{\max}$ , average force  $F_{\text{avg}}$ , the saturation flux point of the lamination material  $B_{\text{sat}}$ , iron ratio  $k_{\text{Fe}}$ , the current density in copper  $J_{\text{Cu}}$ , pole number  $n$ , copper space factor  $k_{\text{Cu}}$ , maximum current of the amplifier  $I_{\max}$ , permanent magnet packing factor  $k_{\text{PM}}$ , coercivity and remanence of the PM used ( $H_c$  and  $B_r$  respectively) and slot dimensions  $b_2$  and  $b_3$ . Most of these depend on the materials used and are thus given by the manufacturers of said materials. The iron ratio is a percentage value which determines how high share of the circumference is used by the iron material varying from 0 (no iron at all) to 1 (solid disk and thus no slots). Space factors indicate how tightly either the conductors of the winding or the permanent magnet pieces are packed in their related spaces. These factors greatly affect the requirements for the manufacturing of the windings and the outer diameter of the AMB.

### 3.1.1 Stator Yoke

With knowledge of the rotor outer radius  $r_{\text{re}}$  and the air gap length  $g_0$  the inner radius  $r_{\text{si}}$  of the stator can be calculated as follows

$$r_{\text{si}} = r_{\text{re}} + g_0 \quad (3.1)$$

Based on the Maxwell stress with the maximum force and the saturation flux density the pole surface area needed can be estimated as

$$A_{\text{pole}} = 2F_{\max} \frac{\mu_0}{B_{\text{sat}}^2} \quad (3.2)$$

Next with the inner radius of the stator, iron factor and the number of poles  $n$  the peripheral length of the pole surface can be estimated as follows

$$l_{\text{pole\_surf}} = \frac{r_{\text{si}} 2\pi k_{\text{Fe}}}{n} \quad (3.3)$$

Now that the surface peripheral length and the area of the pole have been calculated the stack length of the laminated part is calculated as follows

$$l_{\text{stack}} = \frac{A_{\text{pole}}}{l_{\text{pole\_surf}} k_{\text{lam}}} \quad (3.4)$$

Where  $k_{\text{lam}}$  is the lamination space factor. Lastly, the pole width is estimated as follows

$$l_{\text{pole}} = 2 \sin \left( \frac{\pi k_{\text{Fe}}}{n} \right) r_{\text{si}} \quad (3.5)$$

### 3.1.2 Slot Geometry

For determining the required coil area, the average force of the bearing is used

$$A_{\text{coil}} = \frac{F_{\text{avg}} g_0}{A_{\text{pole}} B_{\text{sat}} J_{\text{Cu}} k_{\text{Cu}}} \quad (3.6)$$

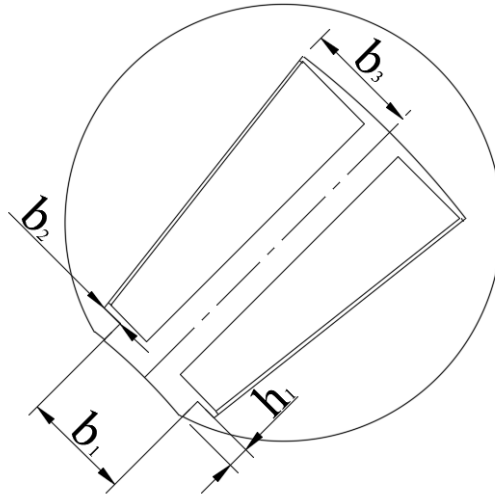


**Figure 3-2** Dimensions of the slot

Of the dimensions presented in the Figure 3-2  $b_2$  and  $b_3$  are input variables. Parameters  $b_1$ ,  $b_2$  and  $b_3$  are connected to each other so that the  $b_3$  is limited to the value that is larger than the value  $b_2 + \frac{b_1}{2}$ . Parameters  $b_1$ ,  $h_1$  and  $r_{\text{slot}}$  can be calculated as follows

$$b_1 = 2 \sin \left( \frac{2\pi(1 - k_{\text{Fe}})}{\frac{n}{2}} \right) r_{\text{si}} \quad (3.7)$$

Where  $n$  is the number of poles. Both  $h_1$  and  $r_{\text{slot}}$  depend on the winding manufacturing. The windings can be wound either along the pole in form of a half circle or as a rectangularly shaped coils so that they do not penetrate in the air gap. The benefit of a winding along the pole is that the overall system becomes more compact, but the winding process becomes more difficult. The following equations are given for case when the winding is wound along the pole.

$$h_1 = r_{\text{si}} \sqrt{2} - \frac{b_1}{2} - \sqrt{r_{\text{si}}^2 - \left( \frac{b_1}{2} \right)^2} \quad (3.8)$$

$$r_{\text{slot}} = \sqrt{\left( \frac{2A_{\text{coil}}}{b_3 + b_2} + r_{\text{si}} + h_1 \right)^2} \quad (3.9)$$

When the winding is wound along the pole  $h_1$  will be the same as  $b_2$  and thus the height of the slot will be a lot smaller.  $b_2$  is connected to  $h_1$  also so that if in general case the  $b_2$  is larger than  $h_1$  they will be set to same value. The maximum width of the coil stack can be estimated as follows

$$l_{\text{coil, end}} = b_3 - \frac{b_1}{2} + \frac{b_1}{4} \quad (3.10)$$

Because the winding is designed so that it will be the widest on the top part of the slot, it needs to be made sure that the winding fits into the slot. To ensure that the coil fits into the slot following condition is set  $b_3 > l_{\text{coil, end}} + 2t_{\text{ins}}$ , where  $t_{\text{ins}}$  is the thickness of the insulation used

in the coils which is provided by the manufacturer of said coils. The thickness of the insulation is typically in range of 0.3 mm. If this condition is not met, the value of  $b_3$  is set to value  $b_3 = l_{\text{coil,end}} + 2t_{\text{ins}} + 1$  mm. This leaves at least 2 mm gap between the coils in the slot which enables air flow for the windings and no risk of contact.

### 3.1.3 Dead Leg

The dead leg is a solid disk and thus the peripheral length of the dead leg is calculated as follows

$$l_d = 2\pi r_{\text{si}} \quad (3.11)$$

For the axial length of the upper part of the dead leg the following equation is used

$$l_{\text{d,up}} = \frac{A_{\text{pole}}}{r_{\text{si}}\pi} \quad (3.12)$$

Because the design illustrated in Figure 2-2 is used the rotor end of the dead leg is widened to decrease the flux density in the air gap. Because the flux density can be calculated as  $B = \frac{\Phi}{A}$ , where  $B$  is the flux density,  $\Phi$  is the flux and  $A$  is the surface area through which the flux travels. It is seen that by doubling the surface area the flux density is halved and thus the axial length of the lower end of the dead leg is calculated as follows

$$l_{\text{d,down}} = 2l_{\text{d,up}} \quad (3.13)$$

### 3.1.4 Permanent Magnet

For the permanent magnet there is a lower limit for the thickness which is predetermined by the manufacturing capabilities. The width of the PM is selected so that it is at least equal to the width of the coil with the margin of 1mm. It is also beneficial to increase the width of the PM as it will reduce the flux leakage as the current linkage increase will be higher than the magnetic voltage drop caused by the increased reluctance. With PM width and magnetic properties of the PM the area of the PM can be calculated

$$S_{pm} = \frac{4B_{sat}A_{pole}}{2\left(B_r - \frac{5B_r g_0}{4H_c l_{pm}\mu_0}\right)} \quad (3.14)$$

Where  $w_{pm}$  is the width of the PM, which is determined above. Equation (3.14)(3.14)(3.14) is based on the following relation set for the permanent magnets (MMPA, 1988)

$$S_{pm} = \frac{B_g A_g}{B_d} \quad (3.15)$$

Where  $B_g$  is the flux density in the air gap,  $A_g$  is the surface area of the air gap and  $B_d$  is the actual flux density of the PM when demagnetization is considered. In this case  $B_g = B_{sat}$ ,  $A_g = A_{pole}$  and  $B_d = 2\left(B_r - \frac{5B_r g_0}{4H_c l_{pm}\mu_0}\right)$ . Upper part is multiplied with the number of poles which is in this case 4.

Because split magnet pieces are used, the space factor of the magnet  $k_{pm}$  is introduced, with it the real value for the magnet area can be calculated as follows

$$A_{pm} = \frac{S_{pm}}{k_{pm}} \quad (3.16)$$

With knowledge of the real area of the PM the external radius of the stator can now be calculated.

$$r_{se} = \sqrt{\frac{A_{pm}}{\pi} + (r_{slot} + l_{yoke})^2} \quad (3.17)$$

Where  $l_{yoke}$  is the distance between top of the slot and the outer edge of the stator, which is predetermined.

### 3.1.5 Coil Parameters

Number of turns can be estimated based on the current linkage needed and, in practice, with the maximum current, air gap length and saturation flux density

$$N = \left( \frac{B_{sat} g_0}{2\mu_0 I_{max}} \right) \quad (3.18)$$

RMS current is estimated with average force

$$I_{rms} = \frac{F_{rms} g_0}{A_{pole} B_{sat} N} \quad (3.19)$$

For estimating the length of the coil, the following equation is used:

$$l_{coil} = 2l_{stack} + \frac{(r_{slot} + r_{si} + h_1) \frac{\pi}{2} N}{2} \quad (3.20)$$

The cross-sectional area of the coil wire can be calculated with copper space factor, number of turns and total area of the coil

$$S_{wire} = \frac{A_{coil} k_{Cu}}{N} \quad (3.21)$$

With length and cross-sectional area of the coil the resistance of the coil can be calculated

$$R_{\text{coil}} = \frac{\rho_{\text{Cu}} l_{\text{coil}}}{S_{\text{wire}}} \quad (3.22)$$

Where  $\rho_{\text{Cu}}$  is the resistivity of copper. The ohmic-losses of the AMB with knowledge of the resistance can be estimated

$$P_{\text{cu}} = 4I_{\text{rms}}^2 R_{\text{coil}} \quad (3.23)$$

Lastly, the inductance of the coil can be estimated

$$L_{\text{coil}} = \frac{N^2 \mu_0 \mu_r l_{\text{stack}} l_{\text{pole}}}{l_{\text{coil}}} \quad (3.24)$$

Where  $\mu_r$  is the relative permeability of the iron material around which the coil has been wound.

The maximum temperature of the control coil depends on the insulation material for example class 155 (F) insulation has the maximum operating temperature of 155 °C guaranteeing at least 20 000 h lifetime. The maximum available current linkage of the coils is dictated by the maximum temperature. In most cases the maximum temperature of the coils is not reached because the AMB must be designed so that it has some overhead during operation to account for dynamic loads. AMBs can also be designed for medium loads so that the maximum temperature can be reached during operation. However, this means that the temperature of the coils must be monitored with a thermal sensor because prolonged maximum control currents can occur because of brief excessive dynamic loads.

### 3.2 Reluctances, Force-Current Factor, and Force-Displacement Factor of the AMB

The starting point for calculating the reluctances is to get some reference values for the flux densities in the air gaps of the AMB. In this chapter, a simplified FEM model is used for getting the said reference values. More detailed evaluation of the analytical model is done in Chapter 5, where 3D-FEM model is used in the verification of the results.



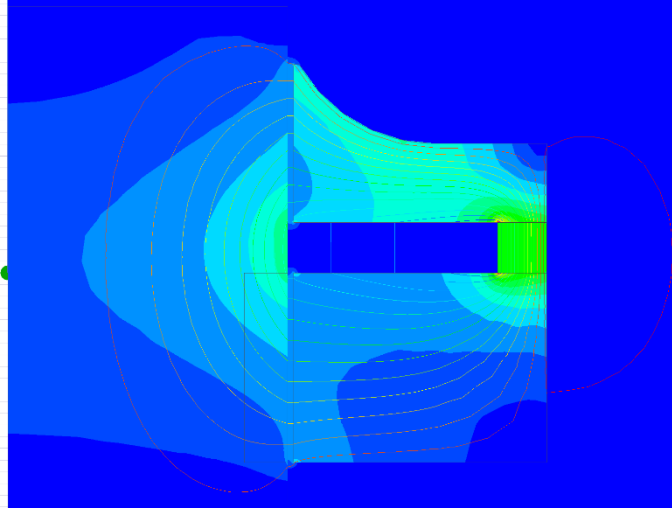


**Figure 3-3** Flux density map of the reference 2D FEM model used in evaluation of analytical calculations of flux densities

The reluctance network of the homopolar AMB with PM-biasing is presented in Figure 2-7. The presented circuit is calculated in parts, gradually adding different reluctances into it to present the effect of different reluctances on the result. Error between FEM values and the analytical values of the flux densities is also followed to evaluate how good the reluctance estimations are. The biggest simplification in the FEM model is that linear materials are used for all parts with the relative permeability of 5000, except permanent magnets.

### 3.2.1 Reluctances of the Air Gaps and of the PM

At first, the reluctance circuit is calculated in its most basic form, without any leakages or fringing. Also, both air gaps are assumed to be fully cylindrical. Reluctances for both gaps and the permanent magnet are calculated as follows

$$R_{m,dl} = \frac{l_{gap}}{\mu_0 S_{gap}} = \frac{\ln(r_{si}/r_{re})}{2\pi l_{d,down} \mu_0} \quad (3.25)$$

$$R_{m,pm} = \frac{w_{pm}}{\mu_{pm} S_{pm}} = \frac{l_{pm}}{\mu_{pm} \pi (r_{pm,o}^2 - r_{pm,i}^2)} \quad (3.26)$$

where

$$\mu_{pm} = \frac{B_r}{H_c} \quad (3.27)$$

$$R_{m,lam} = \frac{l_{gap}}{\mu_0 S_{gap}} = \frac{\ln(r_{si}/r_{re})}{2\pi l_{stack} \mu_0} \quad (3.28)$$

Total reluctance of the first circuit

$$R_{m,cyl} = R_{m,dl} + R_{m,pm} + R_{m,lam} \quad (3.29)$$

Magnetomotive force of the PM

$$F_{pm} = B_r \frac{l_{pm}}{\mu_{pm}} = H_c l_{pm} \quad (3.30)$$

Flux in the circuit and flux densities in middle of each air gap are calculated as follows

$$\phi = \frac{F_{pm}}{R} \quad (3.31)$$

$$B_{lam} = \frac{\phi}{S_{lam}} = \frac{\phi}{2\pi l_{stack} \frac{r_{re} + r_{si}}{2}} = \frac{\phi}{\pi l_{stack} (r_{re} + r_{si})} \quad (3.32)$$

$$B_{dl} = \frac{\phi}{S_{dl}} = \frac{\phi}{2\pi l_{d,up} \frac{r_{re} + r_{si}}{2}} = \frac{\phi}{\pi l_{d,down} (r_{re} + r_{si})} \quad (3.33)$$

With this calculation tens of percent errors are got in the flux densities.

### 3.2.2 Main Leakage Reluctances

On second round the most affecting leakages are added into the circuit which are:  $R_{m,dl\_ac}$ ,  $R_{m,pm,top1}$  and  $R_{m,pm,top2}$

$$R_{m,dl,ac} = \frac{l}{\mu_0 S} = \frac{l_{pm}}{\mu_0 \pi (r_{pm,i}^2 - r_{si}^2)} \quad (3.34)$$

Where,  $r_{pm,i} = r_{slot} + l_{yoke}$ .

For reluctances on top of the magnet, ideas presented for example in (Roters, 1941) are used. That book presents permeance equations for different flux paths through air. In this case only half annulus and half cylinder geometries as presented in Figure 2-6 are considered. As the reluctance is the inverse number of the permeance, these equations can be used for calculating the reluctances. For the reluctance of the half cylindrical area straight on top of the magnet the following equation is formed

$$R_{m,pm,top1} = \frac{1}{0.264\mu_0 l} = \frac{1}{0.264\mu_0 2\pi r_{se}} = \frac{1}{0.528\mu_0 \pi r_{se}} \quad (3.35)$$

For the reluctance of the area top of the previous reluctance an equation for half annulus geometrical shape with a slight modification is used as assumption is that the leakage surfaces on the material surfaces are not equal in width. The following equation for the reluctance  $R_{m,pm,top2}$  is derived

$$R_{m,pm,top2} = \frac{\pi(l_{stack} + l_{d,up})}{2\pi r_{se}\mu_0 \left( l_{stack} \ln \left( 1 + \frac{2l_{d,up}}{l_{pm}} \right) + l_{d,up} \ln \left( 1 + \frac{2l_{stack}}{l_{pm}} \right) \right)} \quad (3.36)$$

With inclusion of these reluctances into the total reluctance and with recalculation of the flux densities a ~10% error margin is achieved when comparing to the FEM-value.

### 3.2.3 Fringing and Reluctance of the Steel Parts

To further tune the model, on the third round the fringing in the air gap and the reluctance of the steel parts are added. For the fringing, a simple approximation of the effective surface area

of the air gap is used where it is increased by the length of the air gap on each side. Fringing reluctances are calculated as follows

$$R_{m, \text{lam, fr}} = \frac{l_{\text{gap}}}{\mu_0 S_{\text{gap}}} = \frac{\ln(r_{\text{si}}/r_{\text{re}})}{2\pi(l_{\text{stack}} + 2g_0)\mu_0} \quad (3.37)$$

$$R_{m, \text{dl, fr}} = \frac{l_{\text{gap}}}{\mu_0 S_{\text{gap}}} = \frac{\ln(r_{\text{si}}/r_{\text{re}})}{2\pi(l_{\text{d, down}} + 2g_0)\mu_0} \quad (3.38)$$

Reluctances of the steel parts are calculated as follows

$$R_{m, \text{dleg}} = \frac{l}{\mu_0 \mu_r S} = \frac{\ln(r_{\text{pm, i}}/r_{\text{si}})}{2\pi\mu_0 \mu_r l_{\text{d, up}}} \quad (3.39)$$

$$R_{m, \text{lamleg}} = \frac{l}{\mu_0 \mu_r S} = \frac{\ln(r_{\text{pm, i}}/r_{\text{si}})}{2\pi\mu_0 \mu_r l_{\text{stack}}} \quad (3.40)$$

$$R_{m, r} = \frac{l}{\mu_0 \mu_r S} = \frac{0.5(l_{\text{d, down}} + l_{\text{stack}}) + l_{\text{pm}}}{\mu_0 \mu_r \pi r_{\text{re}}^2} \quad (3.41)$$

After adding these reluctances into the total reluctance and recalculating the flux densities once again, the error margin drops to ~5%.

### 3.2.4 Side Leakages

With such a low error percentage, one could determine the calculations sufficiently accurate, but as seen in Figure 3-3 there is still some major side leakage on the legs and the FEM-model used for the reference values is very basic and thus it is good to have as accurate analytical answer as possible. Thus, reluctances for these side leakages are added into the calculations.

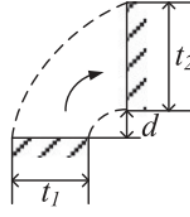


**Figure 3-4** Geometrical parameters for calculating reluctances of two perpendicular walls

The calculation of side reluctances has some uncertainty as the parameters  $t_1$  and  $t_2$  cannot be estimated very accurately and thus a constant value for them is used. Also, the leakage is assumed to be only on one side of the leg. For dead leg, it is assumed that both  $t_1$  and  $t_2$  are 1 mm wide and the  $d$  is the length of the air gap. For the laminated leg, it is assumed that the  $t_1$  and  $t_2$  are 5 mm wide and the  $d$  is still the length of the air gap. In the general, case, the side reluctance is calculated as follows

$$R_{m,side} = \frac{\pi(t_1 + t_2)}{2l\mu_0 \left( t_1 \ln \left( 1 + \frac{t_2}{d} \right) + t_2 \ln \left( 1 + \frac{t_1}{d} \right) \right)} \quad (3.42)$$

Side reluctances are added into the total reluctance and with the recalculation of the flux densities <5% error margin can be achieved.

### 3.2.5 Separation of the Fluxes

All the calculations made above are done with the estimation that the air gap is fully cylindrical on both legs. This is not the case on the laminated part as it has slots for the control coils. To consider these slots the iron factor will be added into the calculations. The air gap reluctance of a single pole is calculated as follows

$$R_{m,lam,pole} = \frac{l_{gap}}{\mu_0 S_{gap}} = \frac{4 \ln(r_{si}/r_{re})}{2\pi k_1 l_{stack} \mu_0} \quad (3.43)$$

At one pole is considered at this point the fringing is analysed in more detail. To do this the fringing is assumed to happen in quarter of a cylinder form and for that an equation from (Roters, 1941) is used. This equation is like the half cylindrical one used for the magnet but as

the leakage path is halved the permeance and thus the reluctance is doubled. Fringing on the axial side of the pole is also introduced as previously only the circumferential side of the pole was considered. These two reluctances are connected in parallel and can be calculated as follows

$$R_{m,fr} = \frac{1}{\frac{1}{0.52\mu_0 l_{stack}} + \frac{1}{0.52\mu_0 l_{pole,surf}}} \quad (3.44)$$

The fringing is connected in parallel to the pole and thus the total reluctance of single pole is calculated as follows

$$R_{m,lam,pole,fr} = \frac{1}{\frac{1}{R_{m,lam,pole}} + \frac{1}{R_{m,fr}}} \quad (3.45)$$

It can be seen from the design that there are four poles in parallel which means that the reluctance is divided by four. By adding the new pole reluctance into the total reluctance and with the new reluctance total the flux densities can be calculated once again and the error percentage drops into 1-2 % range. With the lamination, it can even drop into <1 % error margin. If the lamination effect is wanted to be taken into consideration the flux of the system must be reduced further. Consideration of the laminated material is discussed more in 5.2.3.

There are still some minor parts in the design of which the leakages could be considered. Such part is for example between the magnet pieces as there is a small air gap between them, but in the scope of this work this kind of optimization will be moved into the future if deemed necessary.

### 3.2.6 Force Production and Force-Current and Force-Displacement Factors

After calculating the bias flux for the system, the force production of the AMB can be evaluated. The force production is derived with principle of virtual work as follows

$$F = \frac{(\phi_{\text{lam}} + \phi_i)^2 - (\phi_{\text{lam}} - \phi_i)^2}{2\mu_0 A_{\text{pole}}} = \frac{2\phi_{\text{lam}}\phi_i}{\mu_0 A_{\text{pole}}} \quad (3.46)$$

And the bearing capacity of the AMB can be estimated as follows

$$F_{\text{max}} = \frac{4\phi_{\text{lam}} I_{\text{max}} N}{\mu_0 A_{\text{pole}} R_{\text{tot}}} \quad (3.47)$$

Where  $\phi_{\text{lam}}$  is the flux on the air gap of the active part and  $R_{\text{tot}}$  is the total reluctance of the AMB. This value is considered as an absolute maximum which the system is able produce thus, the requirements of the system must be lower than this value.

The force production of the AMB can also be presented with the force-current and force-displacement factors

$$f_x(i, x) = k_i i_x - k_s x \quad (3.48)$$

These factors are good indicators on how the system behaves in terms of its two main control parameters: displacement ( $x$  or  $y$  depending on the direction) and the control current  $i$ . For the analytical estimation of these factors, equations presented in (Betschon, 2000) are used

$$k_i = \frac{B_{\text{lam}} A_{\text{pole}} N}{g_0} \quad (3.49)$$

$$k_x = -\frac{2}{\mu_0 A_{\text{pole}} g_0} \phi_{\text{lam}}^2 \quad (3.50)$$

## 4. OPTIMIZATION OF THE BEARING

To get better understanding about the design presented in Chapter 3 mathematical optimization to the number of key parameters which affect the performance of the AMB design is performed.

In this chapter, the full description of the optimization procedure is presented with an example in the end.

#### 4.1 Objective Function

The optimal design of a homopolar AMB with PM-biasing starts with setting an objective function. Objective function is the target to which the optimization is performed. If the system has a rotor that is designed as a rigid rotor, system will have a rated working angular velocity point which must be selected so that it is not close to the critical speed. From this, design of the system gets a constraint to follow.

$$\omega_r \leq 0.7\omega_1 \quad (4.1)$$

In which  $\omega_1$  is the first bending critical angular velocity. If there is need for more high-speed rotation, this critical point must be increased. In general, with high-speed machines to influence the bending critical speed the length of the rotor must be considered as it is the most influential factor. In the design of the AMB it must be made sure that the overall axial length of the whole system (motor and AMB) does not increase much with inclusion of the AMB. Because of this, an objective function for the length of the AMB can be written as follows

$$l_{amb} = l_{coil,end} + l_{stack} + l_{pm} + l_{d,down} \quad (4.2)$$

Effect of the length optimization is dictated by the overall construction of the system. In some cases, the AMB can be fitted under the end windings of the electrical motor thus the AMB does not affect the overall axial length of the system.

Another good target for optimization in the system are the aerodynamic losses. These losses affect the overall efficiency of the system and can cause significant temperature rises in the rotor. Methods presented in (Saari 1998) are used to estimate the friction losses in the air gap.

$$P_w = kC_f\rho_{air}\pi\omega^3r_{re}l_{amb} \quad (4.3)$$



Where  $k$  is a roughness coefficient, which is in this case 1, because rotor surface is assumed as a smooth surface.  $\rho_{\text{air}}$  is the density of the air and  $\omega$  is the rotation frequency.  $C_f$  is a friction coefficient which can be estimated as follows

$$C_f = 0.0152 \left( \frac{\mu_{\text{air}}}{\rho_{\text{air}} \omega r_{\text{re}} g_0} \right)^{0.24} \quad (4.4)$$

Third good optimization objective for the system is the copper losses of the windings. This means that the system utilizes as low amount of copper as possible for producing the force required. In AMB systems the force requirement of the system is typically selected by using a value which is ~2-3 times the force of gravity of the shaft and rotor combined.

$$F \sim 2 \dots 3mg \quad (4.5)$$

Where  $m$  is the mass of the rotor and shaft combined and  $g$  is the standard acceleration due to gravity which is in this case set to  $9.81 \text{ m/s}^2$ . Also, because the force production of the system can be presented like in (3.44) a following function for the RMS current of the system can be derived

$$I_{\text{rms}} = \frac{mg}{k_i} \quad (4.6)$$

With the RMS current of the system the copper losses of the system are calculated as follows

$$P_{\text{cu}} = 4R_{\text{coil}} I_{\text{rms}}^2 \quad (4.7)$$

The maximum voltage level is a good target for optimization as the more voltage we can utilize the more power from the amplifier we are able to utilize. The voltage of the two control coils connected in series can be calculated as follows

$$U = 2(R_{\text{coil}} + iL_{\text{coil}}2\pi f_r)I_{\text{max}} \quad (4.8)$$

where  $f_r$  is not the bandwidth of the system in a strict definition as it is an inverse time constant. But as linear system usually reaches steady state in '3 x time constant' it can be said that this value is linearly proportional to the bandwidth of the system. Parameters for the windings are presented in the chapter 3.1.5. When (4.2), (4.3), (4.7) and (4.8) are combined the following multiobjective function can be formed

$$\begin{cases} \min (l_{\text{amb}} = w_{\text{coil}} + w_s + w_{\text{pm}} + w_{\text{d,down}}) \\ \min(P_w = k C_f \rho_{\text{air}} \pi \omega^3 r_{\text{re}} l_{\text{amb}}) \\ \min(P_{\text{cu}} = 4 R_{\text{coil}} i^2) \\ \max U = 2(R_{\text{coil}} + i L_{\text{coil}} \omega_r) I_{\text{max}} \end{cases} \quad (4.10)$$

## 4.2 Optimization Parameters

In this thesis, the iron ratio of the AMB, the rotor outer radius and bandwidth are used as optimization parameters. The iron ratio which is the ratio of iron material versus empty space, affects the axial length of the AMB. Higher iron ratio lowers the axial length of the AMB while increasing the overall diameter of the AMB. Rotor external radius affects the stator external diameter and the aerodynamic losses. With higher bandwidth a higher voltage level can be utilized and the amount of usable power with the maximum control current is increased.

## 4.3 Optimization Algorithm

After declaring the objective function and parameters an optimization algorithm is selected which is used to solve the multiobjective function presented above. In this work, MATLAB and more specifically its Optimization Toolbox, with several pre-built functions, is used to tackle the problem. In the toolbox there are functions like *paretosearch()* and *gamultiobj()* which both utilize optimization a concept called *Pareto efficiency*. *Pareto Efficiency* is a situation where a parameter cannot be improved without making the others worse. *Pareto front* is a set of different pareto efficient results and is typically displayed graphically. More in-depth information about these algorithms can be read from the *MATLAB* documentation (MathWorks 2020). As the optimization problem is by nature nonlinear the convergence to the global optimum is not guaranteed. Thus, minor variation in the results are expected. Also, the algorithms produce only

minimum values and negative values are used for the bandwidth which value needs to be maximized.

In this thesis the *gamultiobj()*-function was decided to be used as it produces more optimized results. At this stage, the increased number of function iterations used to get those results will not be an issue as the calculation time will stay relatively low and the requirement for more calculation power will not be a problem.

#### 4.4 Optimization Example

**Table 1** Input values for the design

Max force [N]	1000
Mean force [N]	750
$B_{\text{sat}}$ [T]	1.100
$\mu_r$	5000
Air Gap [m]	0.001
Current density [A/m <sup>2</sup> ]	4000000
Copper packing factor	0.500
$I_{\text{max}}$ [A]	16
Magnet packing factor	0.800
Coercivity of the magnet [A/m]	860000
Remanence of the magnet [T]	1.130
Slot $B_2$ [m]	0.002
Slot $B_3$ [m]	0.010

Population size used for the optimization algorithm is 60 and the pareto fraction used is 0.7. Bounds for the optimization variables are set as follows

**Table 2** Bounds of the optimization variables

	$L_b$	$U_b$
$k_{\text{FE}}$	0.3	0.9
$r_{\text{re}}$ [mm]	0.025	0.075
$\omega_r$ [Hz]	500	2500

These bounds depend on the application to which the AMB is being designed for. The upper limit of the bandwidth is also dependent on the lamination material used for the AMB as the iron losses of the core material is highly dependent on the frequency. The target rotational speed is set to 20000 RPM, the operation temperature is set to 40 °C and the air density is set to 1.127 kg/m<sup>3</sup>. It should be noted that the level where the rotational speed is set has large impact on the aerodynamic losses. In (4.3), it is seen that the rotational speed is the most affecting variable as it is in power of three.

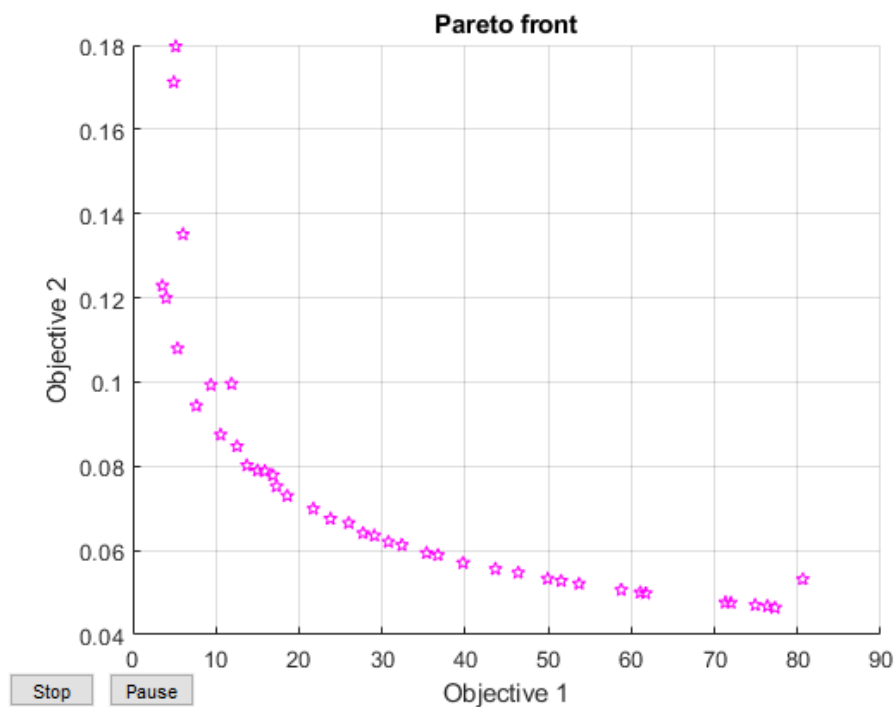


**Figure 4-1** Example of a pareto front produced by the optimization algorithm

As seen in Figure 4-1, the pareto front produced is quite nice. There are barely any divergent pareto points and they set nicely on a curve. This indicates that the performed optimization can be utilized. The total number of function cycles required for the pareto front displayed in Figure 4-1 is 8160.

Pearson's linear correlation coefficients are used to evaluate the optimization result. These coefficients display how different variables correlate with each other. Pearson's correlation coefficients vary between -1 and 1. Correlation is more linear the closer to each end the value is; negative values display negative correlation and positive values vice versa.

**Table 3** Example of Pearson's correlation coefficients

		Output Variables				Input Variables		
		Aerodynamic Losses [W]	Length of The AMB [m]	Copper Losses [W]	Voltage [V]	Iron Ratio	Rotor Radius [m]	Bandwidth [Hz]
Output Variables	Aerodynamic Losses [W]	1.000	-0.788	0.974	-0.785	0.501	0.973	-0.423
	Length of The AMB [m]	-0.788	1.000	-0.888	0.842	-0.836	-0.891	0.412
	Copper Losses [W]	0.974	-0.888	1.000	-0.851	0.614	0.999	-0.452
	Voltage [V]	-0.785	0.842	-0.851	1.000	-0.732	-0.844	0.808
Input Variables	Iron Ratio	0.501	-0.836	0.614	-0.732	1.000	0.598	-0.453
	Rotor Radius [m]	0.973	-0.891	0.999	-0.844	0.598	1.000	-0.438
	Bandwidth [Hz]	-0.423	0.412	-0.452	0.808	-0.453	-0.438	1.000

In Table 3 it can be seen that of the selected input variables, the rotor radius is clearly the most dominating one as it correlates heavily with all the output variables. The rotor radius correlates linearly with the losses, with both aerodynamic and copper losses. The rotor radius has a strong negative correlation with the length of the AMB and the voltage level. The iron ratio also has strong correlation with almost all the output variables though they will be less than with the rotor radius. Bandwidth of the system correlates strongly only with the voltage of the system. As the function is generally non-linear and the correlation coefficients are for a linear system it is determined that the correlations are feasible in some small region of the parameter variations.

In conclusion it can be said that when selecting values for the final design the focus should be on the rotor radius and the iron ratio as they have effect on a wider range of output variables. Depending on the desired output, compromises must be made with the rotor radius as it has both strong negative and strong positive correlation with output variables. In cases where high bandwidth can be a problem, the voltage of the system should be limited. Also, the amplifier used for supplying the AMB sets limitations for the maximum voltage which should be considered when selecting the input bandwidth.

Based on the correlation coefficients following input values for the optimization variables of the AMB are selected:

**Table 4** Optimization variables of the AMB

<b>Optimization variables</b>	
Iron Ratio	0.892
Rotor Radius [m]	0.042
Bandwidth [Hz]	2500

These optimization variables produce following output values:

**Table 5** Optimization results

<b>Optimization result</b>	
Windage Losses [W]	14.914
Length of the AMB [mm]	76.446
Copper Losses [W]	8.391
Maximum Voltage [V]	297.118

With the optimization variables following geometry for the AMB is calculated

**Table 6** Geometry of the AMB

<b>Geometry [mm]</b>	
Pole width	55.400
Stack length	36.300
Coil width	8.200
Yoke inner diameter	146.100
Stator outer diameter	173.900
PM width	9.200
Dead leg width up	15.400
Dead leg width down	30.800
Rotor diameter	84.000
Slot b1	7.300
Slot b2	2.000
Slot b3	10.000
Slot h1	2.000

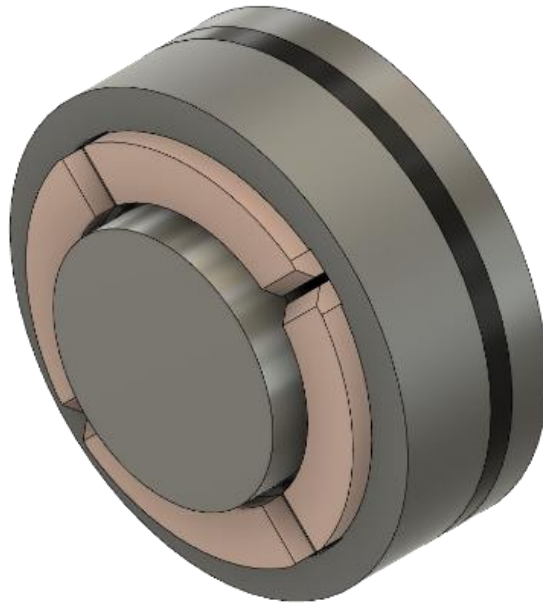


**Figure 4-2** 3D-sketch of the finalized design

Now that there is a 3D model of the design, it can be imported to the *Ansys* -software for more detailed FEM analysis. The 3D model created is used for both 2D and 3D analysis.

## 5. VERIFICATION OF RESULTS WITH FEM

FEM-calculation is used to get more thorough understanding of the AMB. As the system is analysed problems with the initial design might rise. Typical problems with the design include, not having enough bias flux, control flux or force, having too much force and the saturation of either the dead leg or the inner part of the rotor. With the information got from the FEM-calculations the possible problems are assessed with adjusting the geometry of the AMB. If adjusting the geometry does not bring the desired results, then the FEM-model and parameters used there must be investigated. This iterative cycle is continued until the results from the FEM-calculations are within predetermined design criteria. 3D-FEM calculation which produces the most accurate results is time and calculation power intensive and thus should be avoided if possible. One method for reducing the need for the 3D-FEM calculation is presented in the end of this chapter.

### 5.1 Testing the Viability of the Model

After creating the model, a simplified FEM model is utilized to check if the model produces valid results in a variety of test cases. Each test case has some design parameters changed. For each case, the optimization cycle is performed which generates the geometry and analytical values for the flux densities.

For this thesis, four different test cases were chosen. The input values for each case are presented in Table 7 and results are presented in In Table 7 we see that in all the cases maximum bandwidth can be utilized as the rated voltage of the system in this case is 300 volts. Also, the voltage level drops as the force requirements of the system drop and the inductance of the coils decreases.

Table 8. For most of the cases only a few key parameters are changed but for the fourth case multiple parameters were changed. One of the most crucial parameters to vary is the length of the air gap as it is linked to most of the calculations.



**Table 7** Calculation data of the performed tests

	Test 1	Test 2	Test 3	Test 4
<b>Optimization variables</b>				
Iron Ratio	0.892	0.869	0.864	0.871
Rotor Radius [m]	0.042	0.074	0.052	0.029
Bandwidth [Hz]	2500.000	2500.000	2500.000	2500.000
<b>Input variables</b>				
Max force [N]	1000	2000	1000	200
Mean force [N]	750	1500	750	100
$B_{\text{sat}}$ [T]	1.100	1.500	1.100	1.100
$\mu_r$	5000	5000	5000	5000
Air Gap [m]	0.001	0.001	0.0005	0.0005
Current density [A/m <sup>2</sup> ]	4000000	4000000	4000000	4000000
Copper packing factor	0.500	0.500	0.500	0.500
$I_{\text{max}}$ [A]	16	16	16	10
Magnet packing factor	0.800	0.800	0.800	0.800
Coercivity of the magnet [A/m]	860000	860000	860000	860000
Remanence of the magnet [T]	1.130	1.130	1.130	1.130
Slot $b_2$ [m]	0.002	0.002	0.002	0.002
Slot $b_3$ [m]	0.010	0.010	0.010	0.0075
<b>Optimization result</b>				
Windage Losses [W]	14.914	80.446	32.739	1.161
Length of the AMB [mm]	76.446	49.000	64.000	27.000
Copper Losses [W]	8.391	18.260	4.469	1.765
Maximum Voltage [V]	297.118	273.459	140.486	46.908
<b>Post-Processing results</b>				
Coil wire length [m]	2.668	5.768	1.418	1.320
Coil resistance [m $\Omega$ ]	15.300	32.910	8.130	17.840

Coil inductance [mH]	2.463	3.418	1.756	0.930
Added rotor weight [kg]	3.295	6.586	4.246	0.552
Number of turns	28	38	14	22
$k_i$ [N/A]	17.5905	26.622	21.752	3.2692
$k_x$ [N/ $\mu$ m]	7.3281	9.572	23.196	2.8632
<b>Geometry [mm]</b>				
Pole width	55.400	94.600	65.900	37.300
Stack length	36.300	23.000	30.700	10.800
Coil width	8.200	6.100	7.200	6.000
Yoke inner diameter	146.100	229.500	137.800	87.300
Stator outer diameter	173.900	257.600	165.500	103.000
PM width	9.200	7.100	8.200	7.000
Dead leg width up	15.400	9.500	12.600	4.500
Dead leg width down	30.800	19.000	25.200	9.000
Rotor diameter	84.000	148.000	104.000	58.000
Slot $b_1$	7.300	15.400	11.200	6.000
Slot $b_2$	2.000	2.000	2.000	2.000
Slot $b_3$	10.000	10.000	10.000	7.500
Slot $h_1$	2.000	2.000	2.000	2.000

In Table 7 we see that in all the cases maximum bandwidth can be utilized as the rated voltage of the system in this case is 300 volts. Also, the voltage level drops as the force requirements of the system drop and the inductance of the coils decreases.

**Table 8** Flux density values and the error between calculations

<b>RESULTS</b>					
		Test 1	Test 2	Test 3	Test 4
<b>Maxwell references</b>	$B_{lam,ref}$	0.318	0.313	0.371	0.280
	$B_{dl,ref}$	0.376	0.376	0.451	0.333
<b>Calculation results</b>	$B_{lam}$	0.322	0.314	0.374	0.281
	$B_{dl}$	0.384	0.385	0.459	0.346
<b>Error %</b>	Lamination	1.289 %	0.319 %	0.809 %	0.393 %
	Dead leg	2.074 %	2.394 %	1.774 %	3.904 %

In Table 7 we see that in all the cases maximum bandwidth can be utilized as the rated voltage of the system in this case is 300 volts. Also, the voltage level drops as the force requirements of the system drop and the inductance of the coils decreases.

Table 8 it is seen that the error percentage between FEM and analytical analysis stays relatively low in each test case. The sudden increase in the dead leg error percentage for the fourth case is most likely an under estimation of the side leakages as the width value used for them is an educated guess as the accurate estimation of them is difficult. Despite that, the results indicate that the calculation model created is valid as the error is only ~1-3% in most cases.

One way to modify the analytical model closer to the FEM results is to modify the permeability of the materials used. This means adding the effect of the bandwidth and thus effect of the eddy currents into the permeability. The following equation can be used for estimating the effect of the eddy currents on the permeability (Meeker et al. 1996)

$$\mu_{rf} = \mu_{r,lam} \frac{\tanh\left(\sqrt{i\sigma_{lam}\mu_0\mu_{r,lam}} \frac{d}{2}\right)}{\sqrt{i\omega_r\sigma_{lam}\mu_0\mu_{r,lam}} \frac{d}{2}} \quad (5.1)$$

Where,  $\sigma_{lam}$  is the conductivity of the laminated material, which in turn is the inverse number of the resistivity of the material.  $\mu_{r,lam}$  is the static value of the permeability (in this case 5000) and  $d$  is the thickness of the single lamination layer. Most of these values are given by the manufacturer of the material. Transformation presented in (5.1) lowers the initial permeability value and cut couple points of percentages from the error.

## 5.2 Static 3D FEM Analysis of the Homopolar AMB with PM Biasing

As stated before, at base level a simplified 2D-FEM model is utilized for evaluating the results of the analytical calculations. In this chapter a 3D-FEM analysis is performed to check if the estimations on the flux densities are valid. Also, more complex material properties are added

into the FEM model as it increases the accuracy of the FEM calculations. A parametric sweep is performed on the system to determine the capabilities of the system. For the calculations Ansys software is used.

As a base for the FEM model, the 3D-model created in Chapter 4.4 is used. Materials used were: Sura M270-35A, for the laminated parts (stator and rotor), S355J structural steel for the dead leg and the shaft and permanent magnet selected was Neorem 595a.

The Sura M270 starts to saturate around 1.5 T. The frequency/loss model for the M270 is also implemented as provided by the manufacturer. At first, the space factor is set to 1 with the M270 as using realistic values complicates the calculations considerably and increases the calculation time significantly. The space factor 1 makes it so that the flux of the system is distributed more evenly.

S355J structural steel is selected for the dead leg as there is not any special requirements for it and structural steel is widely available. Neorem 595a is selected because it has good coercivity and remanence and for this application higher temperature grade is not required from the magnet. As the materials selected are middle-of-the-road but still in range of the design, the material expenses will stay in line and thus, they are good candidates for real life application.

Flux densities are calculated for each air gap. Also, the inductance of the coil is calculated. For the parametric sweep, the control current and displacement of the rotor are varied as they determine the force affecting the rotor. Five points for each parameter is used for total of 25 variations.

### 5.2.1 Bias flux in the system

At first, the bias flux distribution in the gaps is calculated. This can be done with model that does not include the windings. Also, for this part a  $\frac{1}{4}$  of the total model can be used without fear of losing accuracy.

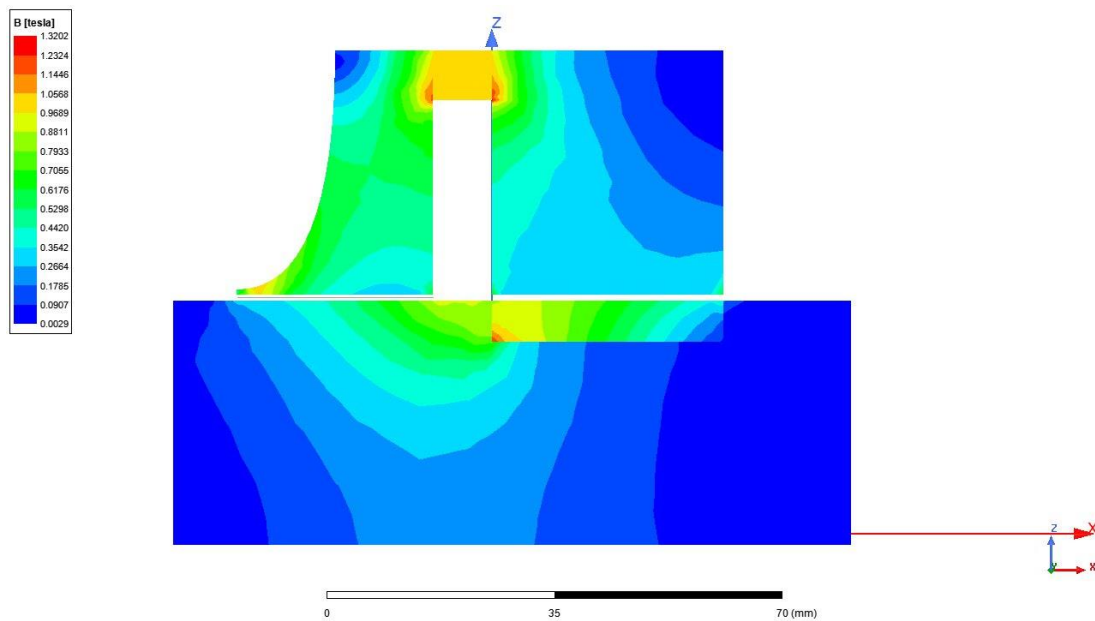


**Figure 5-1** Flux density distribution inside the stator presented as axial cut of the full model.

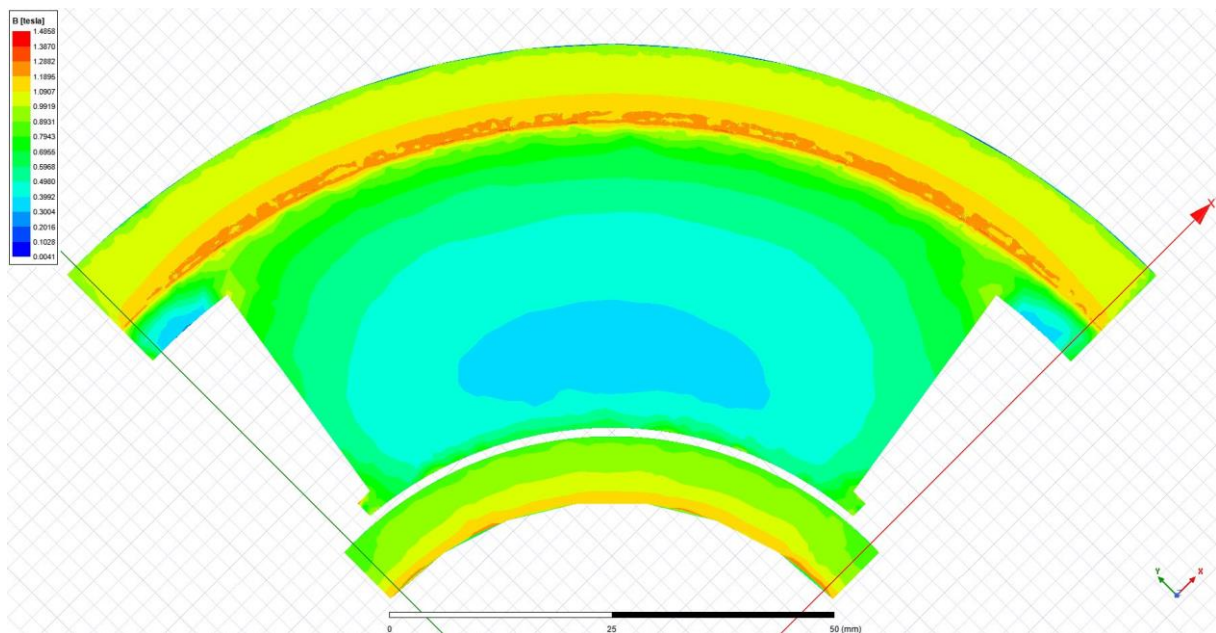


**Figure 5-2** Radial cut view of the flux density distribution inside the stator and rotor

In Figure 5-1 and Figure 5-2 it is seen that the flux inside the stator travels the shortest route inside the materials. Therefore, the flux density builds up just after the PM which gradually fades away along the axial direction. Also, most of the flux travels next to the slots in the radial direction and there are “cold” spots in the middle of the poles. Despite all, the flux densities are on a level of the input value ( $B_{\text{sat}} = 1.1 \text{ T}$ ) it is a bit over in some places.

The flux densities on the dead leg are on the level where the structural steel starts to saturate. The saturation of the dead leg brings a couple benefits with it. First one is that the bias flux becomes less dependent on the temperature changes. This is because the bias flux will be for the most part be controlled by the saturation flux density of the dead leg material which is way less temperature dependent than the flux generated by the PM. The second benefit of the saturated dead leg is that it will contribute less on the negative stiffness of the system as the total flux of the dead leg air gap does not increase as much as with the non-saturated leg when the rotor displacement changes. (Filatov et al. 2016)

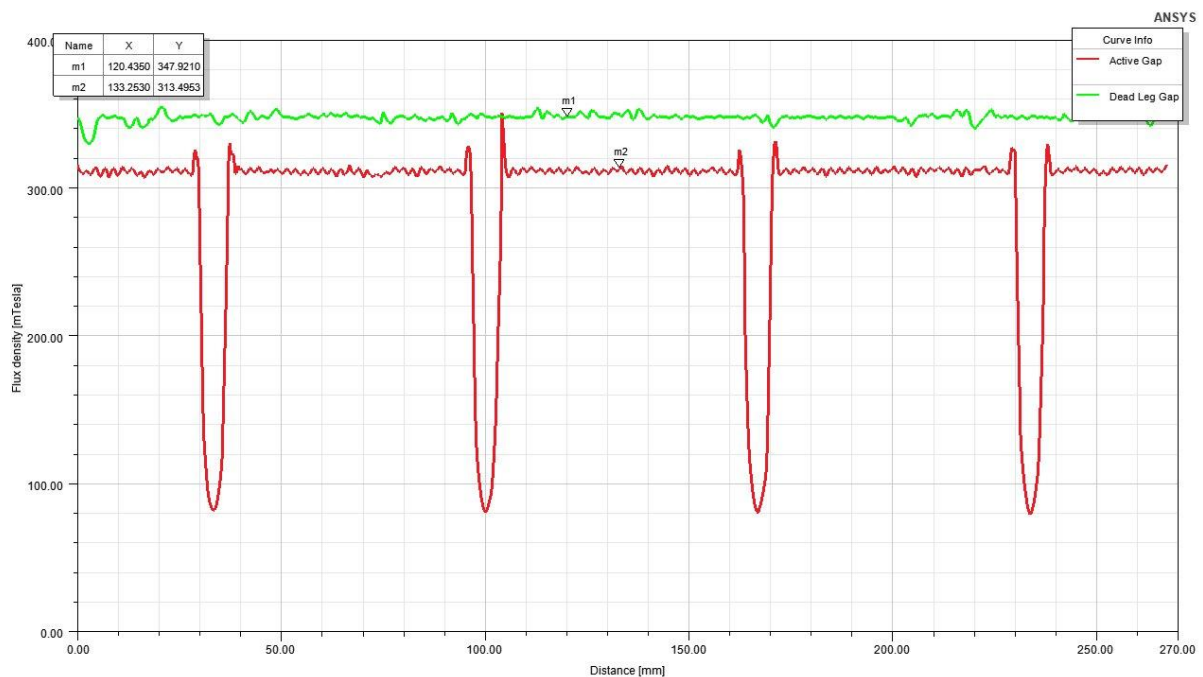


**Figure 5-3 Flux densities in both air gaps**

In Figure 5-3 the effect of the slots on the active gap flux density can be seen clearly. Also, there is flux build up on the slot edges which further tells that the flux travels on the edges of the material. For analysing the analytical model based on the information in Figure 5-3 Flux

densities in both air gaps following flux density values are selected:  $B_{\text{lam,ref}} = 0.313 \text{ T}$  and  $B_{\text{dl,ref}} = 0.348 \text{ T}$ . With these values the error between FEM and analytical model sets to  $\sim 2 \%$  for the active part and  $\sim 9 \%$  for the dead leg part.

### 5.2.2 Bearing capacity of the AMB

For calculating the forces in the system, the full 3D-model must be used. This is because the FEM-calculations consider the full model even when split to  $\frac{1}{4}$ th. For example, with the displacement it would be applied in all the directions in 2D-plane. Also, windings of the system are reduced to singular coil to reduce interference during the calculations. This reduction can be done because the shape of the coil does not affect the result.

The bearing capacity is analysed in one direction as the forces would be identical when varied in either direction. This means that the side coils can be removed from the model and the displacement is varied in z-direction only.

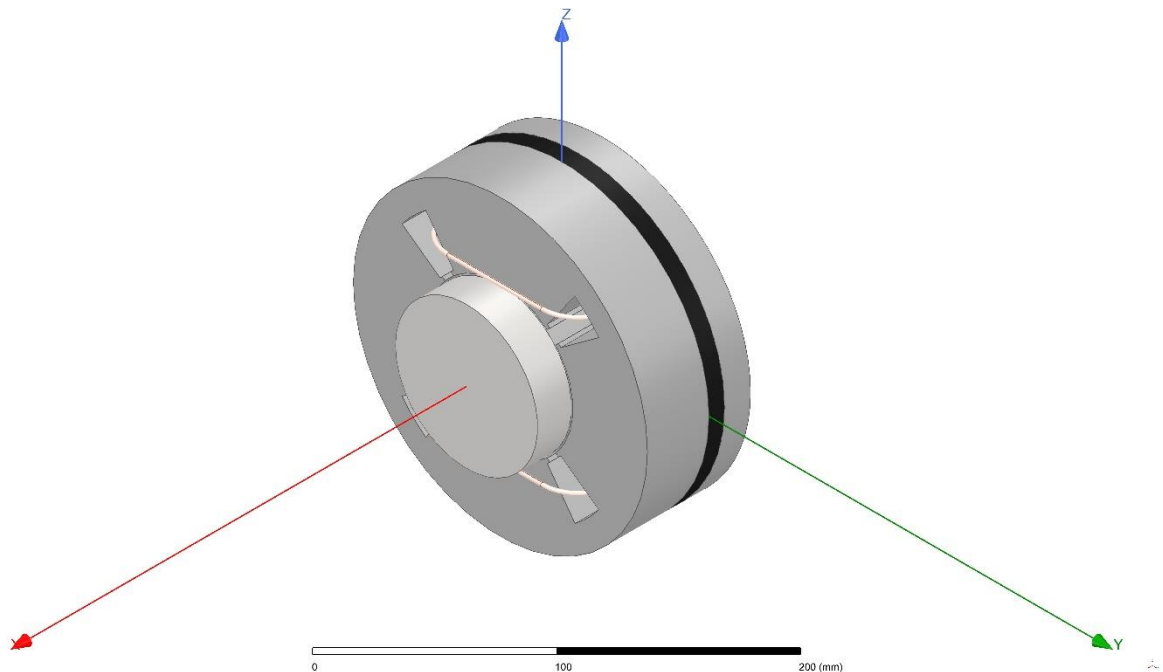


**Figure 5-4** 3D-model used for the parametric analysis

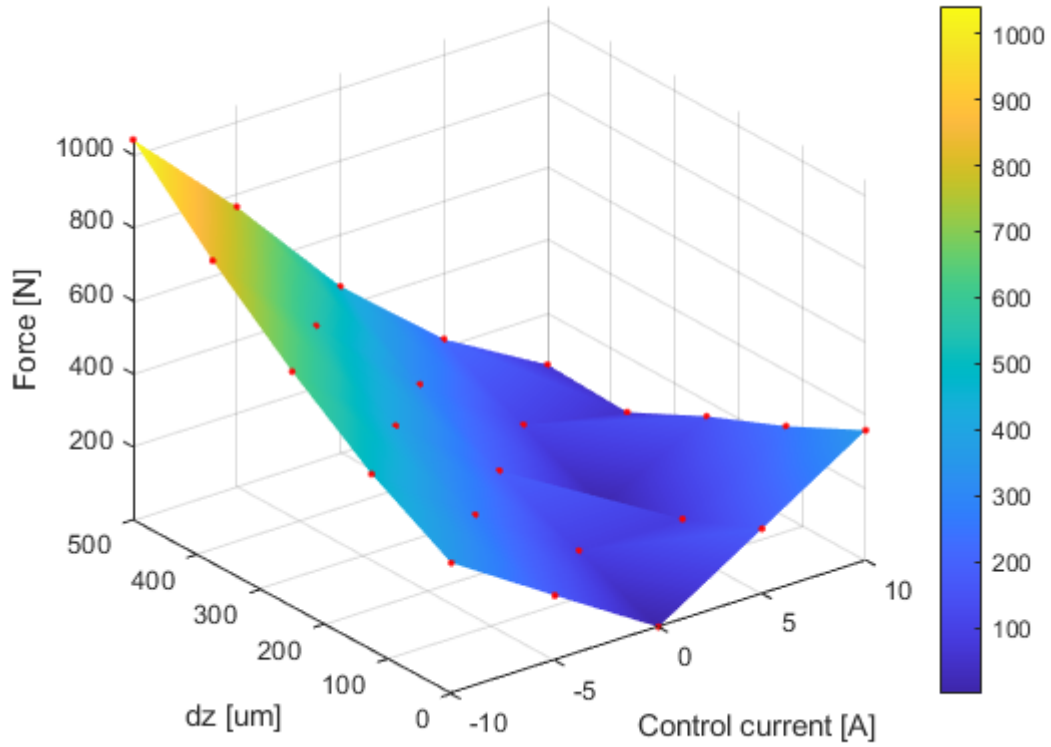


**Figure 5-5** Force production of the AMB with different rotor displacements and control currents presented as a surface plot

As to be expected the maximum carrying capacity of the AMB is reached with maximum control current and maximum displacement. The maximum force is reached with current of  $I_c = -10$  A. In this case  $500\text{ }\mu\text{m}$  is selected as maximum displacement as it is significant displacement of the rotor with 1 mm air gap. Current was varied between -10 and 10 A. The force maximum reached here is in range of the analytically calculated value which further proves the viability of the analytical model.

The inductance of the coils is also calculated with the within the parametric sweep and the resulting  $\sim 2\text{ mH}$  with zero displacement which is the about same result as with the analytical calculation.



### 5.2.3 Laminated material

To fully simulate the laminated material a space factor of 0.95 must be included within the material. Space factor is the ratio between metal and total lamination stack thickness in laminated material. As the model simulates laminated materials the most visible part is that the flux density will vary a lot more in the axial direction as the insulation layers drive the flux to travel even closer to the permanent magnet.

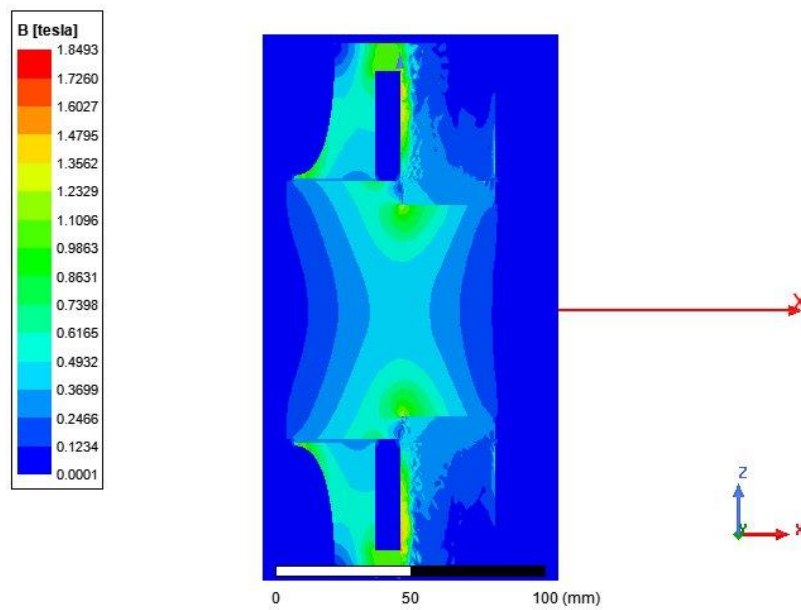


**Figure 5-6** Flux density inside the AMB

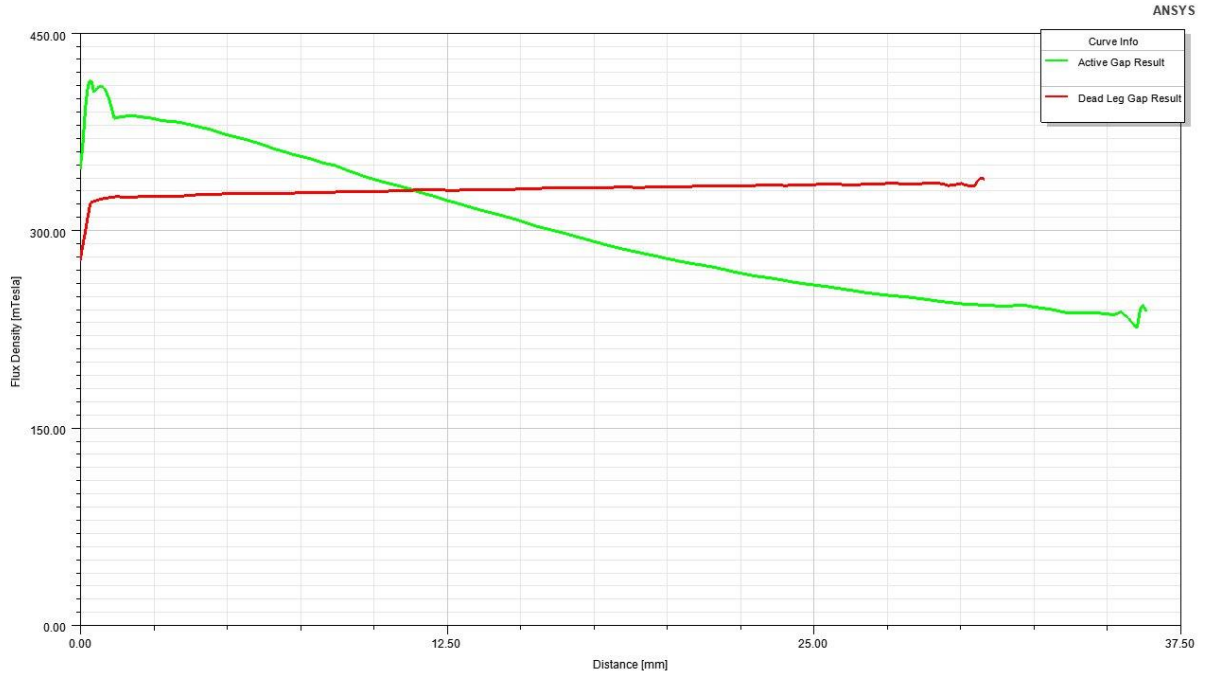


**Figure 5-7** Axial distribution of the flux density

In the analytical model this effect can be taken into consideration by reducing the flux of the system by multiplying it with the space factor. If average values for both are used ( $B_{lam,ref} = 0.300$  T and  $B_{dl,ref} = 0.331$  T) and the space factor is applied into the analytical model ~1 error-% is got for the lamination and ~9 error-% for the dead leg.

### 5.3 Measures Needed to Avoid 3D-FEM Analysis

AMB analysed in this thesis is by its nature a 3D problem because of the rotational non-symmetry of the control pole caused by the winding slots. Because 3D FEM analysis is much more intensive in terms of calculation capacity and time a 2D solution of the model, if possible, is much more desirable. One method for such transformation can be found in (Filatov et al. 2004).

In that paper, a pole factor  $K_{pole}$  is introduced which is the ratio between length of the iron part and total circumference of certain radius  $r$ . In this work, the pole factor is called the iron factor. The flux density  $B$  in a cylinder with radius  $r$  will be higher by the factor of  $1/K_{pole}$ . With higher flux density, the field strength  $H$  will also be higher and thus the magnetic voltage drop on the

laminated pole with slots and air gap. For the reluctances of the laminated pole and air gap the  $BH$ -curve of the medium must be modified

$$H^*(B^*, r) = H \left( B \frac{1}{K_{\text{pole}}(r)} \right) \quad (5.2)$$

This transformation ensures that net fluxes identical magnetic voltage drops in both 3D and 2D models. Transformation works especially in cases where the  $B(H)$ -curve is linear. For example, the air gap flux density changes from  $B = \mu_0 H$  to  $B = \mu_0 / K_{\text{pole}} H$  where the  $K_{\text{pole}}$  is calculated with stator inner radius  $r_{\text{si}}$ . This transformation changes the initial  $BH$ -curve so that it has lower saturation point and the overall curve is shorter

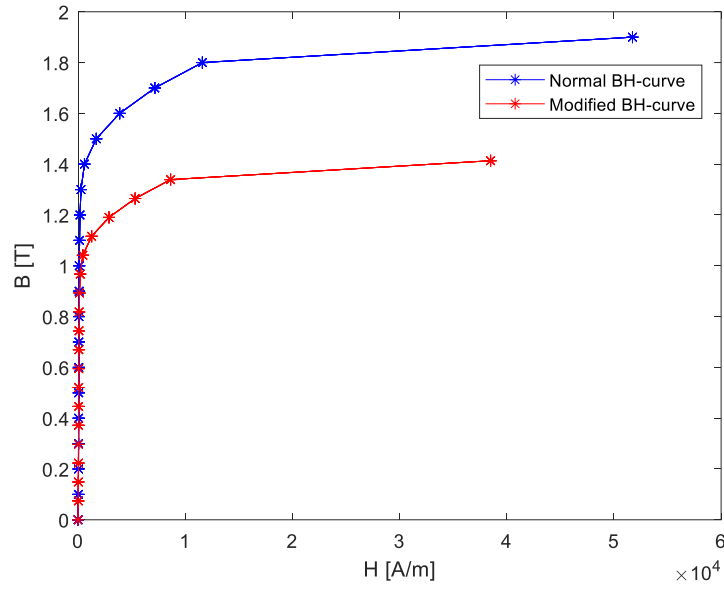


**Figure 5-8** Normal and modified  $BH$ -curve plotted side by side

For the lamination material a modified space factor  $k_{\text{fe}}$  is used, which is the ratio between solid material and the total stack with insulation layers. With modified space factor, the effect of slots can be considered when performing 2D FEM analysis

$$k_{\text{fe}}(r) = 1 - \frac{1 - k_{\text{fe}}}{K_{\text{pole}}(r)} \quad (5.3)$$

From (5.3), it is seen that the space factor is a function the radius  $r$  because  $K_{\text{pole}}$  varies with the radius. In the model, this dependency is best reflected by dividing the slot portion of the stator into several areas with the different radius and thus different values for the  $k_{\text{fe}}$ .

After completion of the FEM calculations in 2D form, the air gap flux density must be transformed back to 3D system value

$$B_{\text{bias}} = \frac{B_{\text{bias}}^*}{K_{\text{pole},0}} \quad (5.4)$$

Where  $B_{\text{bias}}^*$  is the resulting bias flux of the air gap got from 2D FEM model and  $K_{\text{pole},0}$  is the pole factor on the air gap level.

The implementation of this method into the FEM-software is easiest to do by dividing the model into several parts. For each part, a new radius value is used when calculating the material parameters. Also, the pole factor/iron ratio must be calculated for each point used as it changes with the geometry of the slot.

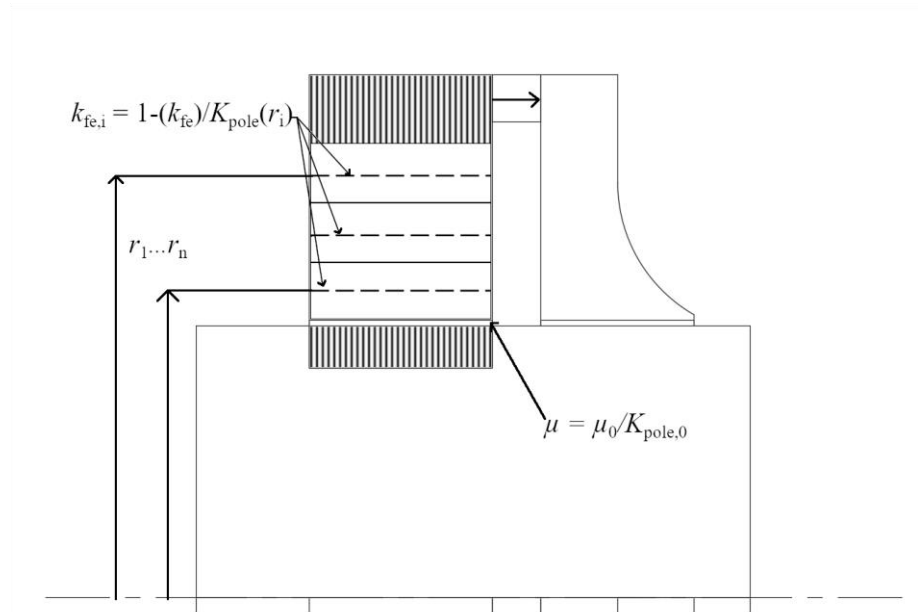


**Figure 5-9** The idea behind dividing the laminated material into sections, with the help of which the winding slots are taken into account (Filatov et al. 2004)

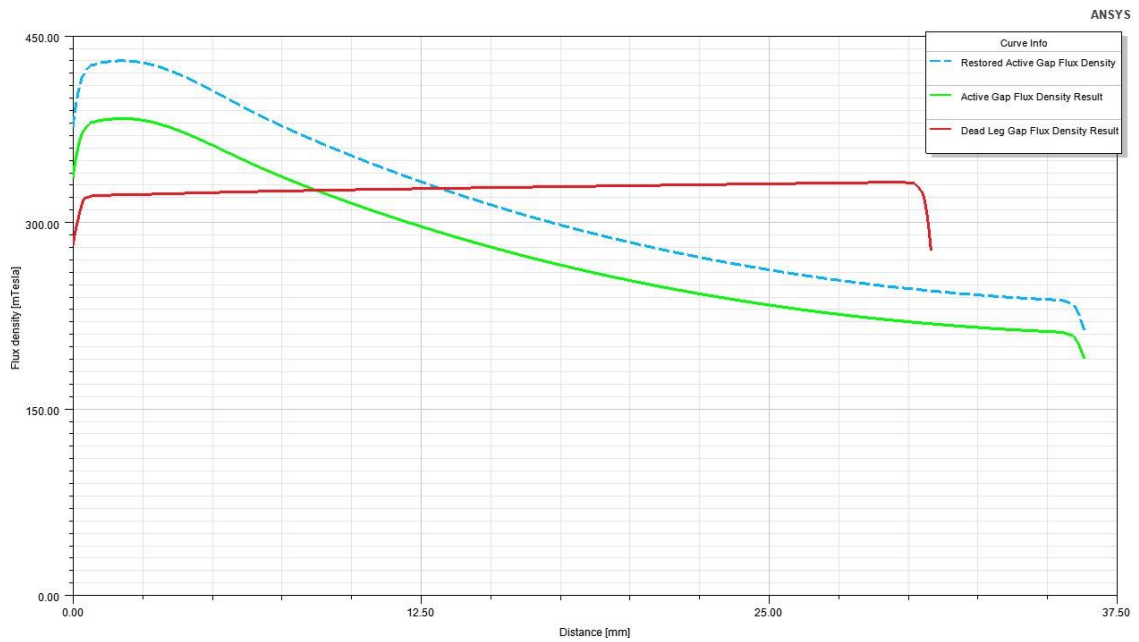


**Figure 5-10** Bias flux density distribution in the air gaps. Where the blue dashed line presents the restored value of the active gap flux densities

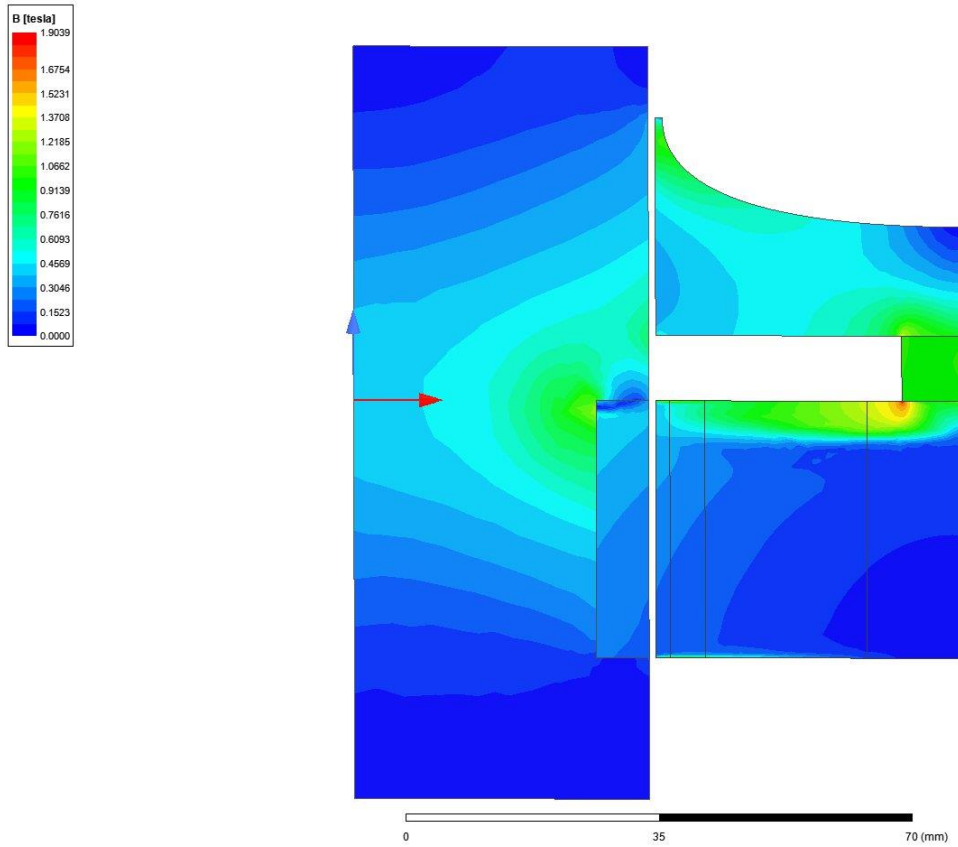


**Figure 5-11** Flux density overlay on the modified 2D-FEM model

As seen in Figure 5-10, the flux density distribution is highly non-uniform. This is because the flux tries to travel along the shortest route which goes in the permanent magnet side of the pole. Figure 5-10 also shows the difference which transformation (5.4) makes on the flux density values. In this case the difference between the values is a couple of tens of mT. As there are no changes on the solid steel material, its flux density distribution is uniform.

If an average value for air gap flux densities is selected ( $B_{lam,ref} = 0.311$  T and  $B_{dl,ref} = 0.327$  T) and they are compared with the 3D-model ones calculated in 5.2.3 there will be ~3 % difference with the active gap flux densities and ~1 % difference with the dead leg gap flux densities. As seen from Figure 5-7 and Figure 5-10 the flux density distributions for the active gap are similar. As the 2D-FEM calculations are by nature simpler, the resulting curve will be smoother. This difference in the calculation accuracy is the most likely reason for the slight difference in the values.

Figure 5-11 displays the fact that most of the flux travels in only a few millimetres wide area. Figure 5-11 shows that the flux density inside the materials stays below the saturation limit selected (1.1 T). The flux density build-up is apparent on the borders where there is a sharp turn and major change in material reluctance, in this case the flux densities grow up to 1.7/1.8 T.

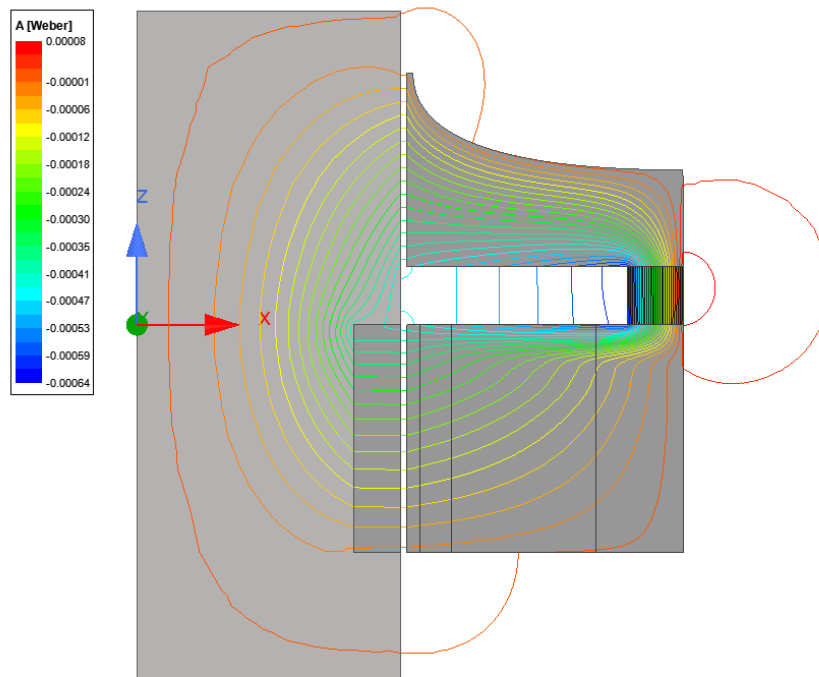


**Figure 5-12** Flux lines inside the materials

Based on Figure 5-12 it can be concluded that the reluctance calculations performed in 3.2 include all the major leakages of the system. Figure 5-12 also shows that there is underestimation on the side leakages and recalculation of them is one of the more effective ways to reduce the error percentage in the flux further.

### 5.3.1 Calculation of Negative Stiffness

Even with considering the winding slots, the calculation of negative stiffness is still a 3D problem. Measures for transforming the negative stiffness calculation into a 2D problem are presented in (Filatov et al. 2004). In that paper, the force created by the bias flux is separated

into two parts: stator part and dead leg part,  $F_s$  and  $F_d$ . This analysis method enables the calculation of forces affecting the rotor with different displacements of the rotor.

$$F_s = \frac{\sum_{i=1}^4 K_{2i}}{(\sum_{i=1}^4 K_{1i})^2} \left( \frac{1}{l_{\text{stack}}} \right)^2 \phi^2 \int_0^l u(x) dx \quad (5.5)$$

$$F_d = \frac{1e}{2\mu_0 2\pi r_{\text{re}} l_{\text{d,down}} \sqrt{g_0^2 - e^2}} \phi^2 \quad (5.6)$$

Where  $K_1$  and  $K_2$  are mathematical coefficients which are expanded more in the source material,  $u(x)$  is the magnetic voltage drop in the lamination in the axial direction divided by the average magnetic voltage drop in the pole,  $e$  is the displacement and  $\varphi$  is the polar angle. With knowledge of the forces, the total force and negative stiffness of the system can be calculated.



## 6. CONCLUSIONS AND SUGGESTIONS FOR FUTURE WORK

The goal in this thesis was to derive an analytical model which can be used for calculating the geometry and the main parameters of an active radial magnetic bearing actuator with PM-biasing and get it to a reasonable error percentage when compared to a more complex FEM-calculations. It can be said that the goal has been reached as the result from the analytical model has maximum error of ~10% which was the original goal set at the beginning.

The analytical model provides with the geometrical dimensions for the AMB which can be used for constructing a 3D-model of the system. This 3D-model can also be used as a basis for the FEM-calculations. Also, within the analytical model the reluctances of the magnetic circuit are calculated and with them the bias flux densities in tow air gaps are calculated. The bias flux densities are then used for calculating the carrying capacity of the AMB. Some system parameters are also calculated which include the winding parameters (length, diameter, number of turns, resistance, copper losses, and inductance of the coil), force-current-and force-displacement-factors.

Besides the analytical model, an optimization procedure was created which was used to optimize some key factors of the system. These factors include the length of the AMB, aerodynamic losses, copper losses and bandwidth of the system. Values of these were used to select the most suitable design for situation and the finalized results for the geometry of the AMB were calculated.

After optimizing the geometry of the AMB, a FEM-analysis of the system was performed to verify the results got from the analytical model. Multiple FEM-calculations was performed with varying simulation accuracy. As a result, a maximum error of ~10 % within the flux density calculations was achieved and especially with the active gap the error dropped as low as 2.5 %. With the inductance and carrying capacity estimations results were close with the analytical model. Also, a way to avoid 3D-FEM calculations was introduced. The results got with it were promising as the difference with it and the 3D-FEM calculation was only a couple of percent with calculation effort being a small fraction of the 3D-FEM. Issue with it was that the

initialization of the model requires a lot of manual input as the different material sections had to be input separately.

For future work, suggestion is to perform more fine-tuning of the model to bring the error percentage down even more. One such way is to transform the reluctance network into matrix form and calculating fluxes for each reluctance component which enables a more detailed analysis of each component. With knowledge of fluxes in different reluctance branches the  $BH$ -curves of the steel materials could also be utilized to calculate multiple values for the permeability. Also, investigation for transition between MATLAB and Ansys to be automated so that the transition especially to the optimized 2D-calculation model would not require much manual input.

## SOURCES

Betschon, F. 2000. *Design principles of integrated magnetic bearings*.

Filatov, A., Hawkins, L. & McMullen, P. 2016. Homopolar Permanent-Magnet-Biased Actuators and Their Application in Rotational Active Magnetic Bearing Systems. *Actuators*, 5(4), p. 26. doi:10.3390/act5040026

Filatov, A. V. & Hawkins, L. A. 2014. Comparative Study of Axial/Radial Magnetic Bearing Arrangements for Turbocompressor Applications. *14th International Symposium on Magnetic Bearings*, 6. Linz.

Filatov, A. V., McMullen P. T., Hawkins, L. A. & Blumber E. 2004. Magnetic bearing actuator design for a gas expander generator. *Ninth International Symposium on Magnetic Bearings, August 3-6, Lexington, Kentucky, USA*.

F. R. Ismagilov, V. E. Vavilov and I. F. Savakhov, "Research of Magnetic Fields in New Design of Homopolar Magnetic Bearing," *2018 XIV International Scientific-Technical Conference on Actual Problems of Electronics Instrument Engineering (APEIE)*, Novosibirsk, 2018, pp. 141-148, doi: 10.1109/APEIE.2018.8545711.

MathWorks. 2020. *Multiobjective Optimization documentation*. Available: [mathworks.com/help/gads/multiobjective-optimization.html](https://www.mathworks.com/help/gads/multiobjective-optimization.html). Accessed 7 July 2020.

Meeker, D., Maslen, E. & Noh, M. 1996. An augmented circuit model for magnetic bearings including eddy currents, fringing, and leakage. *IEEE Transactions on Magnetics*, 32(4), pp. 3219-3227. doi:10.1109/20.508385

Magnetic Materials Producers Association (MMPA). 1980. *Permanent magnet guidelines*. Available: [https://allianceorg.com/pdfs/MMPA\\_Magnet\\_Design\\_Guide.pdf](https://allianceorg.com/pdfs/MMPA_Magnet_Design_Guide.pdf) Accessed 23 July 2020.

Roters, H. 1941. *Electromagnetic Devices*. John Wiley & sons, Ltd. New York. pp. 131-134.

Saari, J. 1998. Thermal analysis of high-speed induction machines. *Acta Polytechnica Scandinavica, Electrical Engineering*, 90, pp. X1-60.

Schweitzer, G. & Maslen, E. H. 2009. *Magnetic bearings: Theory, design, and application to rotating machinery*. Heidelberg: Springer.